Master thesis in physical oceanography

A quantitative description of the West Spitsbergen Current by combining hydrography, altimetry and in-situ current meters

Håvard Muus Falck
June, 2014

Geophysical Institute
University of Bergen
Norway

University Centre in
Svalbard, UNIS
Norway

Acknowlegements

First of all I would like to thank Frank Nilsen, my main supervisor who gave me the opportunity to spend another year on Svalbard. I am sure I owe you a red pen, a blue pen, a pencil, and a holiday. I would also like to thank Marius O. Jonassen for reading through the manuscript towards the end, and fortunately providing digital comments saving me another pen. The discussions with Eli Anne Ersdal, Eva Falck, and Ragnheid Skogseth are also greatly appreciated, and have definitely improved the quality of the work.

I am in also truly thankful for the effort made by Wilken-Jon von Appen at the Alfred Wegener Institute, Bremerhaven, for calculating and providing current data from the AWI mooring array.

Abstract

In a warming Arctic Ocean (AO) it is important to study its main source of oceanic heat and salt. Here, seasonal climatological sections of the West Spitsbergen Current (WSC) across 78.83°N have been constructed using hydrographic data from 1956 to 2013. They have proven to replicate the large scale features of the barotropic branch and the eastern baroclinic branch of the WSC. However, the eastern baroclinic branch is not fully resolved in this section as the sections western boundary is too far east. Three anomaly periods within the data set are defined (1956-2003, 2004-2007, 2008-2013) and presented in order to study the warm anomaly detected in the middle of the 2000s. Surface temperatures exceeding 3 °C in combination with an upward displacement of the Atlantic Water (AW) core were revield in the winter warm anomaly section. A significant increase in the buoyancy of the AW was detected during the summer warm anomaly. These two factors may have a significant impact on the sea ice cover in the AO.

An approximation of the pressure driven surface velocity v_s has been calculated from in-situ current meters (v_s^c) and compared to the surface velocity calculated from altimetry (v_s^a). The latter is found to be too strong with a mean velocity of $0.22\,\mathrm{m\,s^{-1}}$ compared to the mean v_s^c equal to $0.10\,\mathrm{m\,s^{-1}}$. The horizontal shape of v_s^a was not comparable to approximations to the barotropic jet of the WSC found in literature. Based on the hydrographic sections, in-situ current meters and altimetry, the summer and the winter volume transports (V_T) was calculated for the eastern baroclinic and the barotropic branch. The volume transport estimated from v_s^c (V_T^c) was underestimated (1.2 to 1.8 Sv for summer and 0.6 to 1.6 Sv for winter) due to the chosen grid. By extrapolating the geostrophic velocity to the lost data area V_T^c was nudged upwards in the range of 0.3 to 0.4 Sv. The winter V_T of AW was found to increase through the three periods with a distinct peak of 4.4 Sv during the second period (2004 to 2007). After the warm anomaly period the mean temperature of the AW was not seen to decrease to pre-anomaly values. For summer the decrease was 0.3 °C from the second to the third period, and for winter the temperature increased further by 0.1 °C. As a consequence of the observed increase in AW mean temperature in combination with the steady volume transport may continue to warm the Arctic.

CONTENTS

CHAPTER 1

INTRODUCTION

The main flux of oceanic heat and salt into the Arctic Ocean (AO) is carried with the West Spitsbergen Current through the Fram Strait (FS) (Mosby, 1962; Aagaard and Greisman, 1975). Its analogue, the East Greenland Current (EGC), contributes to the mass balance of the AO by transporting colder and fresher Polar Water (PW) out through the FS. These two currents are the primary contributors to the heat and salt budget of the AO (Rudels, 1987; Schlichtholz and Houssais, 1999). On its way into the AO the WSC experiences substantial exchange of heat with both adjacent water masses and the atmosphere. Melting of sea ice also influences the heat content of the WSC, but to a smaller extent. The WSC is mainly guided northwards by topography from its source, the North Atlantic Current (NAC). This topographic steering indicates strong barotropic component of the WSC (Teigen et al., 2010). Vertical movement of the WSC core, however, is mainly driven by changes in buoyancy (Boyd and D'Asaro, 1994).

The WSC can be separated into two main branches, each branch stemming from a different NAC branch in the Norwegian Sea. The two branches are driven by different mechanisms. Figure 1.1 shows a schematic overview of the currents in the FS and adjacent seas. The eastern branch is a prolongation of the highly barotropic Norwegian-Atlantic Slope Current (NwASC) trapped to the Norwegian Shelf Edge. North of Northern Norway the NwASC splits into two branches, about 60 % flowing northward towards the FS, while the rest heads eastward into the Barents Sea. Originating from the Norweigan-Atlantic Frontal Current (NwAFC), following the Mohns and Knipovich Ridges, the western branch of the WSC is mainly baroclinic (Orvik and Niiler, 2002; Skagseth et al., 2004; Walczowski et al., 2005). Between 76 and 78°N these two beanches merge due to the involute bathymetry of the FS (Walczowski et al., 2005). Jakobsen et al. (2003) used lagrangian drifters, and found that the confluence between the two branches happened close to 78°N.

North of this convergence zone, the WSC spilts into three branches; the Return Atlantic Current (RAC), the Yermak Branch (YB) and the Svalbard Branch (SB), see Figure 1.1. The RAC branch flows westwards between 76 and 81°N with about 22 % of

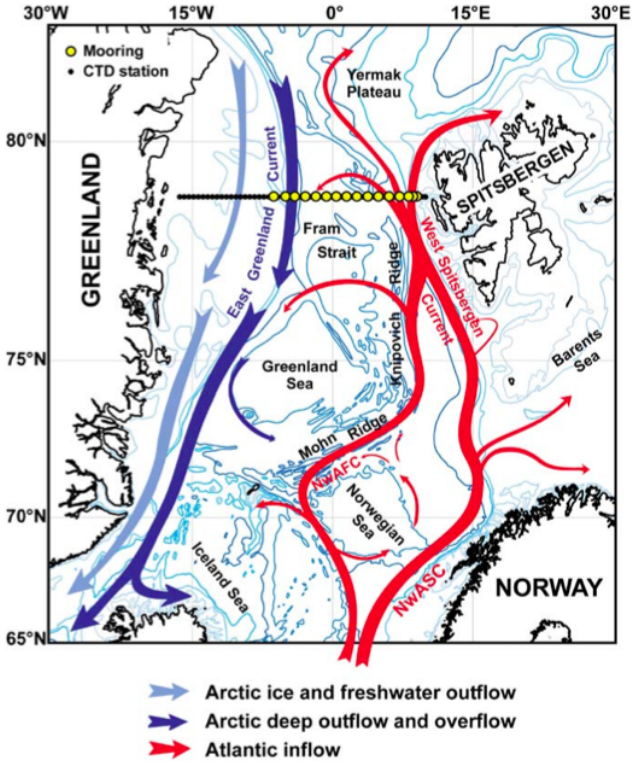

Figure 1.1: Map showing the Fram Strait and the Norwegian Sea. An overview over the WSC and the EGC plus abbreviations are also given (Beszczynska-Möller et al., 2012).

the AW, and is eventually included into the EGC (Manley, 1995). Different pathways between the WSC and the EGC have been suggested within this latitudinal interval (Bourke et al., 1988; Manley, 1995; Fahrbach et al., 2001; Jakobsen et al., 2003; Walczowski and Piechura, 2007). Some of the paths between the WSC and EGC are suggested to go along the Molloy Deep, and crossing the Hovgaard Fracture Zone. The middle branch, YB, flows northward towards the Yermak Plateau (YP). From here it follows the Yermak Plateau Slope (YPS) northwest before it is steered into the AO. The YB experiences substantial modification due to tidal mixing close to the YP. 45 % of the available AW is transported with this branch(Kowalik, 1994; Manley, 1995). The last and easternmost branch of the WSC is the SB. Instead of following the YPS, the current flows northward across the YP. Manley (1995) reported that 33 % of AW carried with the WSC is included in the SB. After crossing the plateau, it turns eastwards trapped to the continental slope enclosing the Eurasian Basin. Further, a portion of the SB is flowing south into the Barets Sea after passing Svalbard (Lind and Ingvaldsen, 2012).

The colder and fresher Spitsbergen Polar Current (SPC) is found shoreward of the WSC(Helland-Hansen and Nansen, 1909). The SPC starts at Sørkapp. In this area the current is known as Sørkappstrømmen or The South Cape Current. Numerical studies show that tidal currents are very strong ($> 1\,\mathrm{m\,s^{-1}}$) in the area south of Sørkapp, and Sørkappstrømmen is subject to extensive tidal mixing (Gjevik et al., 1994; Kowalik and Proshutinsky, 1995). The characteristics of the SPC are not properly described in literature, but it is suggested that it stems from Storfjorden, where it may flow

counter clockwise along the shore line (Skogseth et al., 2005). Sill overflows from Storfjorden is also expected to modify the WSC to some extent (Quadfasel et al., 1988; Skogseth et al., 2005). The transition zone between the WSC and the SPC is known as the Polar Front (PF), and can be seen as a deepening of the pycnocline in the fresh surface layer (Upper 50 m). The location of the PF along the western border of the Barents Sea and the west coast of Spitsbergen was suggested by Loeng (1991).

To monitor the exchange between the Greenland, Iceland and Norwegian Seas (GINS) and the AO, a mooring array was deployed in 1997 across the FS. The array is maintained in collaboration between The Alfred Wegner Institute (AWI) and The Norwegian Polar Institute (NP). See Figure 1.1 for the geographical positions of the moorings. Originally the western part of the array was placed along 78.83°N covering the transport out of the AO via the EGC. The eastern part of the array covering the WSC was placed along 79.00°N (Schauer et al., 2004; Beszczynska-Möller et al., 2012). In 2002 the array was rearranged so all moorings now align along 78.83°N, and two additional moorings were deployed in the center of the FS.

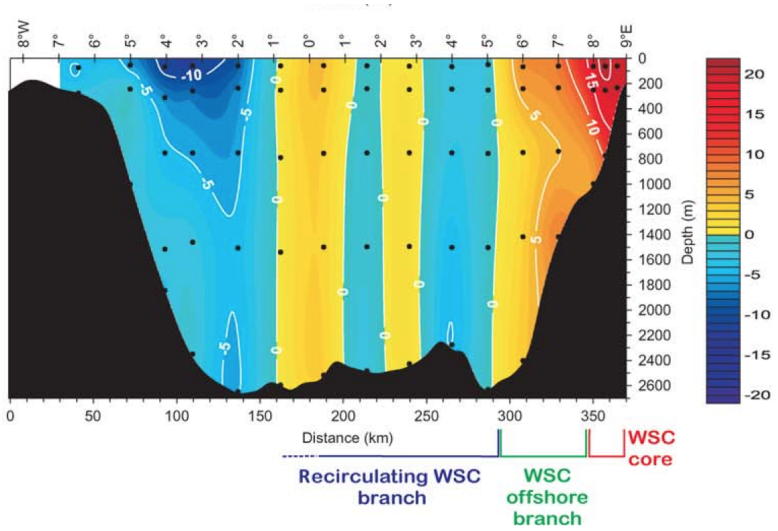

Figure 1.2: Mean cross section velocity [cm s^{-1}] measured by the AWI mooring array across the FS in the period from 2002 to 2008. The black dots indicate current meter positions. Figure adopted from Beszczynska-Möller et al. (2012)

Fahrbach et al. (2001) estimated a volume flux of 9.5 ± 1.4 Sv northward and 11.1 ± 1.7 Sv southwards through the whole FS array. These calculations yield a southward net transport of 4.2 ± 2.3 Sv. Updated values were presented in Schauer et al. (2004) with a similar southward net transport between 4 ± 2 and 2 ± 2 Sv in the period 1997 to 2000. Further monitoring across the whole of the FS gave a volume transport of 12 Sv northward and 14 Sv southward, yielding a southward net transport of 2 Sv (Schauer et al., 2008). Rudels et al. (1994) assign the residual northward flux of 2 Sv to AW inflow into the Barents Sea, and similar results are presented by Rudels et al. (2008). Isolating the volume transport of the WSC, the mean (northward) transport over the period 1997-2010 was 6.6 ± 0.4 Sv. Of this 3.0 ± 0.2 Sv was identified as AW with a temperature above 2 °C (Salinity was not used), and the Atlantic Water mean temperature was 3.1 °C (Beszczynska-Möller et al., 2012).

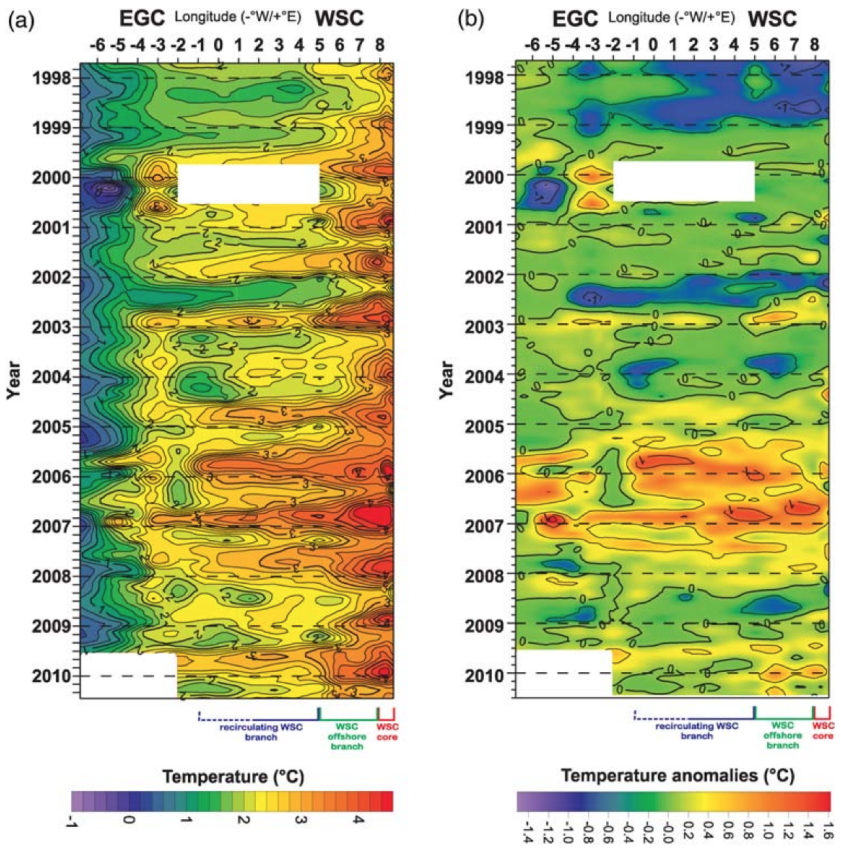

Figure 1.3: Time series from the mooring array along 78.83°N showing monthly means of (a) temperature and (b) temperature anomaly from mean seasonal cycle. The heat flux maximum between 2004 and 2007 is well represented (Adopted from Beszczynska-Möller et al. (2012).)

The mooring array has also been used to study buoyancy reducing processes in the WSC, and to quantify heat loss through horizontal diffusion mechanisms. Using the easternmost moorings in the array (F0 to F7), Teigen et al. (2010) and Teigen et al. (2011) studied barotropic and baroclinic instabilities in the WSC. The first study addressed the velocity shear between the barotropic branch of the WSC and shoreward waters. A skewed gaussian jet profile was used to approximate the barotropic current, and a numerical stability analysis using this jet showed that the barotropic part of the WSC had experienced a shear strong enough to cause instabilities between December 2007 and May 2008. It was further showed that the most stable longitudinal position of the current maximum was close to Mooring F2 (8.4°E). Moving the current maximum towards the shelf break (8.7°E) cause the current to become unstable. During two of the investigated unstable periods the shoreward heat transport corresponded to between 50 to 60 % of the observed local heat loss.

Schauer et al. (2008) showed an increase in heat transport from 26 to 36 TW from 1997 to 1999, through the FS. This increase in heat transport was most prominent in summer, when the temperature maximum of the WSC was measured to have increased with 1 °C through the 9 year period from summer 1997 to 2006. Figure 1.3 shows the complete time series from 1997 to 2010 with monthly averaged tempera-

ture and temperature anomaly. The winter temperature maximum was also observed to have increased, but only with a fraction of the summer maximum. In the period from 1997 to 2010 Beszczynska-Möller et al. (2012) calculated a linear warming trend for the AW mean temperature to be $0.06\,^{\circ}\mathrm{C\,yr^{-1}}$. A similar trend in volume transport was not demonstrated. A similar trend in heating of the WSC core at 79°N was described by Ivanov et al. (2012). Data from the Arctic and Antarctic Research Institute (AARI) from 1979 to 2011 showed that the WSC cores temperature had increased with more than 1 °C. Analysis of the AW layer from the 1950s to 2010 shows increased temperatures in the whole of the Arctic Ocean during the 1990s and 2000s referring to 1970s. A warming trend was also detected in the Fram Strait of $0.062 \pm 0.001\,^{\circ}\mathrm{C\,yr^{-1}}$ (Polyakov et al., 2012). Two heat anomalies were detected using the mooring array along the Svinøy section in the NwASC, one in December 1997 and one in February 2003 (Orvik and Skagseth, 2005; Polyakov et al., 2005). The same anomalies were found in the mooring array along 78.83°N in the FS in 1999, and 2004 (Polyakov et al., 2005; Beszczynska-Möller et al., 2012; Polyakov et al., 2012). Furthermore, the first of these two heating pulses was also detected in February 2004 by a McLane moored profiler located at the central Laptev Sea slope (78.46°N,125.66°E) (Polyakov et al., 2005).

Mork and Skagseth (2010) used altimetry and hydrographic data to quantify the NwAC, and compared the calculated velocities to independent in-situ current meters along the Svinøy section west of Norway. A mean volume transport of 5.1 ± 0.3 Sv for the NwAC was estimated, where the easter branch accounted for 3.4 ± 0.3 Sv while the western branch transported 1.7 ± 0.2 Sv. A significant seasonal cycle in volume transport was also seen, with the winter maximum transport almost twice as large as the summer minimum.

The section across the WSC (78.83°E) constitute the northward extension of the NwAC flowsthrough the Svinøy section. With the same type of data, this work has been motivated by the methods used in Mork and Skagseth (2010) with the objective to quantify the WSC by using altimetry and hydrographic data. This work is part of the UNIS lead project *Remote Sensing of Ocean Circulation and Enviromental Mass Changes* (REOCIRC, RCN, project number: 222696/F50), which aim to apply state of the art instrumentation and theory to study remote sensed ocean circulation and heat fluxes towards the AO. This work has two main goals: The first is to establish a climatological reference section for the hydrography across the WSC, and to detect the warm anomaly of the mid 2000s. Secondly, to calculate the volume transport through the FS following the method of Mork and Skagseth (2010). With a good reference in the in-situ current meters of the AWI mooring array (Beszczynska-Möller et al., 2012), the quality of the altimetric measurements will be assessed the high Arctic. This will be done by first presenting relevant theory and the hydrographic data, the current meter data, and altimetry data available in Chapter 2. Then the results and calculations will be presented in Chapter 3 with suggestions to a climatological state of the hydrography in the WSC and volume transports. Finally in Chapter 4 the results will be discussed and the reliability of the climatology and the volume transport will be addressed.

CHAPTER 2

THEORY, DATA, AND METHOD

2.1 Theory

Geostrophic velocity (v_g)

In Hunegnaw et al. (2009) the Mean Dynamic Topography (MDT) was estimated using both ship, airborne and satellite gravimetry. Calculating volume transports by using this MDT with a long time series of hydrographic data from the Svinøy section proved good results. The transport was calculated to be 3.9 Sv which is close to the 4.2 Sv Orvik et al. (2001) calculated from current meter observations. The method to determine geostrophic surface velocities based on altimetry was further developed by Mork and Skagseth (2010). The geostrophic relation can be represented by

$$\mathbf{u_g} \equiv \mathbf{u_s} + \mathbf{u_{bc}}. \tag{2.1}$$

where $\mathbf{u_g}$ is the total horizontal geostrophic current, $\mathbf{u_s}$ is the surface current driven by surface elevation, and $\mathbf{u_{bc}}$ is the component driven by the horizontal density gradient. By assuming a strictly northward current, leaving the v-component to be perpendicular to the current cross section, the geostrophic current in the **j**-direction comes from

$$v_g(z) = \quad v_s \quad + \quad v_{bc} \tag{2.2}$$

$$= \frac{1}{\rho_0 f}\frac{\partial p}{\partial x} + \frac{g}{\rho_0 f}\int_z^0 \frac{\partial \rho}{\partial x}\,\mathrm{d}z \tag{2.3}$$

where ρ_0 is the reference density of $1028\,\mathrm{kg\,m^{-3}}$, f is the Coriolis parameter $1.43\times10^{-4}\,\mathrm{s^{-1}}$, and g is the gravitational pull of the earth equal $9.83\,\mathrm{m\,s^{-2}}$. Integrating the hydrostatic pressure ($\mathrm{d}p/\mathrm{d}z = -\rho g$) over the Absolute Dynamic Topography (ADT) and inserting into (2.3), we get

$$v_g(z) = \frac{g}{f}\frac{\partial}{\partial x}\mathrm{ADT} + \frac{g}{\rho_0 f}\int_z^0 \frac{\partial \rho}{\partial x}\,\mathrm{d}z. \tag{2.4}$$

Now (2.4) can account for the full depth-dependent geostrophic current. v_s represent now the northwards surface velocity forced by surface elevation. Two different surface velocities will be estimated, one from in-situ current meters and one from altimetry data. They will respectively be referred to as v_s^c and v_s^a, c denoting current meter, and a denoting altimetry.

Volume transport

Upon knowing the water velocity of a current as well as its horizontal and/or vertical extent it is possible to calculate the volume of water transported, i.e. volume transport, V_T. This is obtained by integrating the known velocity over the area it represents, A. The volume transport is then given as

$$V_T = \int_A v_g \, \mathrm{d}A \tag{2.5}$$

where A may represent both a water column, horizontal distance or a current section area. In oceanography volume transport is given in Sverdrup ($1\,\mathrm{Sv} = 10^6\,\mathrm{kg\,m^{-3}}$).

Topographic steering

The conservation of potential vorticity is an important result in geophysical fluid dynamic. It can be written as

$$\frac{\mathrm{d}}{\mathrm{d}t}\left(\frac{f+\xi}{h}\right) = \frac{\mathrm{d}}{\mathrm{d}t}\left(\frac{\text{Vorticity}}{\text{Depth}}\right) = 0 \tag{2.6}$$

where f is the planetary vorticity, ξ $\left(= \partial v/\partial x - \partial u/\partial y\right)$ is the relative vorticity, and h is the depth of the water column. The equation describes the relation between a water column's height and vorticity. If the column is squeezed (i.e. h decreases) its vorticity must equally decrease to preserve the ratio between them. As the result is derived from the nonlinear, frictionless, and barotropic horizontal momentum equation it can be used in the description of the eastern branch of the WSC. Performing a simple scaling analysis with the parameters in Table 2.1 reveals $f/h = constant$ as the dominating part of (2.6). This ratio is often referred to as topographic steering as it shows that for no changes in f, the water column must move along constant bathymetry.

Table 2.1: Scales for (2.6).

f	$1.4 \times 10^{-4}\,\mathrm{s^{-1}}$	X	$1 \times 10^4\,\mathrm{m}$
V	$0.15\,\mathrm{m\,s^{-1}}$	H	$500\,\mathrm{m}$

2.2 Hydrographic data

One of the objectives of this work is to construct a climatological mean for the WSC core along the AWI/NP mooring array, (along 78.83°N). The CTD profiles used for the calculation was collected between 1956 and 2013 , and was kindly provided by the

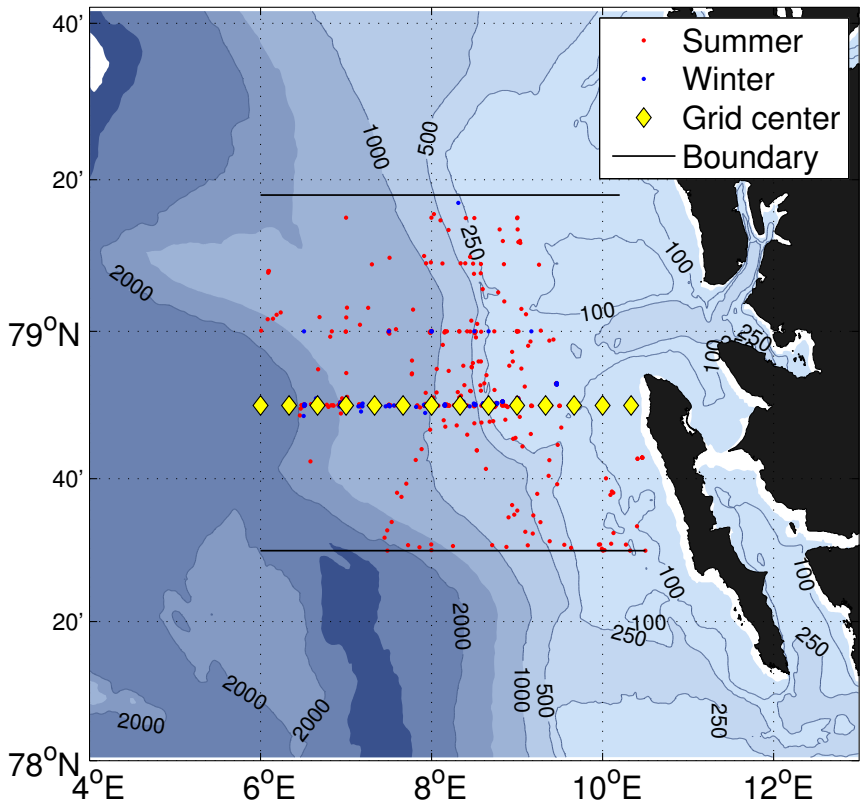

Figure 2.1: Map showing the positions of all CTD profiles used for the climatology. Red and blue dots are summer and winter data respectively. The centered grid used is marked by yellow diamonds, and the black lines are the latitudinal boundary.

PANGAEA database maintained by AWI, the IMR database, and UNIS. The latitudinal boundaries for profiles used is within 78.5 to 79.3°N, and the longitudinal boundary is from 6 to 10.3°E. The longitudinal resolution of the grid was chosen to be 1/3°, the same as the resolution of the ADT grid. Due to the proximity of the Kongsfjorden-Krossfjorden trough, which is expected to be affected by these fjord systems internal processes (Svendsen et al., 2002), profiles within the trough are removed. Large temporal and spatial variations in temperature and salinity can be expected in the upper few meters of the surface layer. When in addition the depth of where the CTD begins sampling also varies (usually within the upper 10 m) the upper 8 m of all profiles have been removed. This is done to dampen the possible spike created by lack or misrepresented data.

Figure 2.1 displays all CTD stations used in this work. The climatological grid is defined such that each grid cell has its center at the yellow diamonds in Figure 2.1. This same grid is used for the ADT/MDT grid. Using the same grid makes it easy to compare the calculated velocities from both altimetry and hydrography. With the latitudinal boundaries defined by the black lines in Figure 2.1, the maximum distance between a grid center and a CTD station's position is approximately 55 km. The distance is calculated using the Haversine formula on a spherical earth with a radius of 6371 km. As most of the profiles used are located much closer to their respective grid centers (mean distance from a profile to its respective grid center is 9 km.), a simple

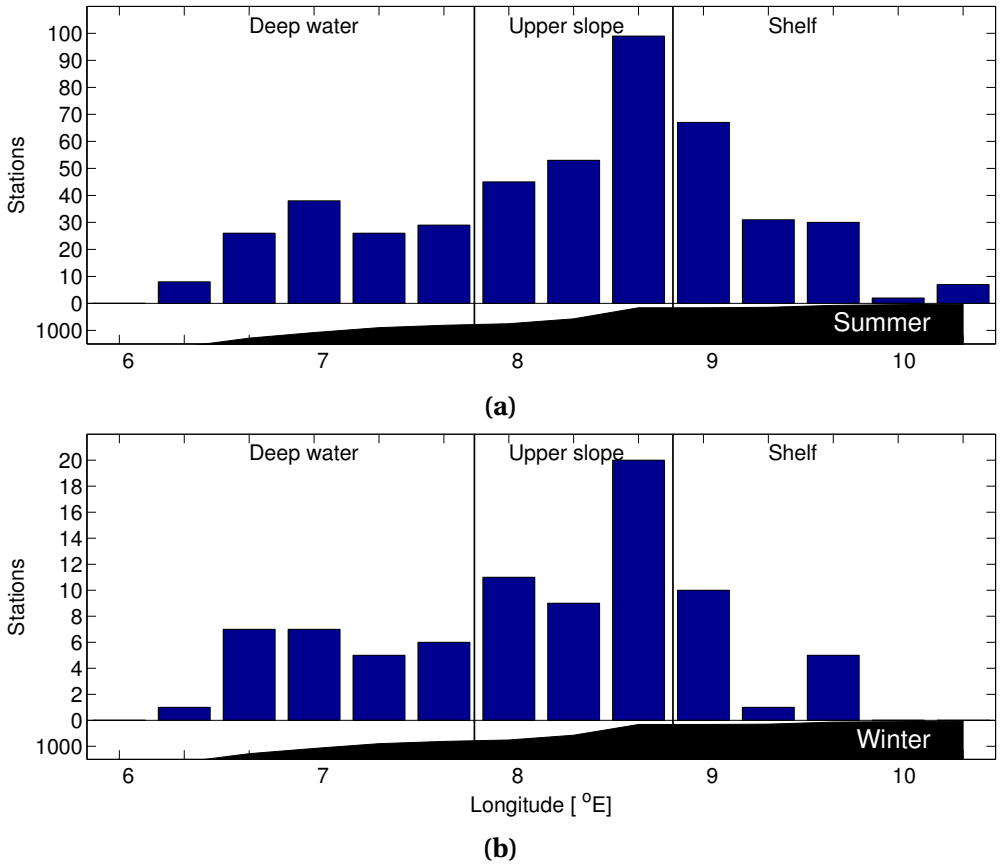

Figure 2.2: Longitudinal distribution of CTD stations per grid point. (a) shows data for summer and (b) shows for winter. Note the difference in scale on the y axis between summer and winter.

arithmetic sample mean is used when calculating the final climatology. The northward heating and freshening gradients calculated by Saloranta and Haugan (2004) for the WSC core give that the change in temperature and salinity along Spitsbergen is in the order of $10^{-1}\,100\,\mathrm{km}^{-1}$. This yields only a very small contribution as the spatial extent of the study area is small.

The longitudinal distribution of profiles used to construct the respective climatologies is seen in Figure 2.2, where a, and b represent summer and winter respectively. The months chosen for summer are June, July, August, September, and October, while the winter months are December, January, February, March, April, and May. These periods will hereafter be referred to respectively as *jjaso* and *djfmam*. It shows that the main body of profiles are collected over the upper slope and just onto the shelf in water deeper than 250 m. Over the deep water and close to shore fewer profiles were collected. Both summer and winter have a similar relative distribution along the section, with the maximum and minimum of profiles over the same areas. However, the winter climatology with its 82 profiles has less than $1/5$ of the 461 summer profiles. This low availability causes some problems when calculating the climatological sections, and it is particularly prominent over the shelf. For instance if only one or two profiles are used to calculate a mean, the result is sensitive to annual variations, and the result is not necessarily a good climatological representation. Profiles older than mid 80s are generally not conducted with high vertical resolution as many of

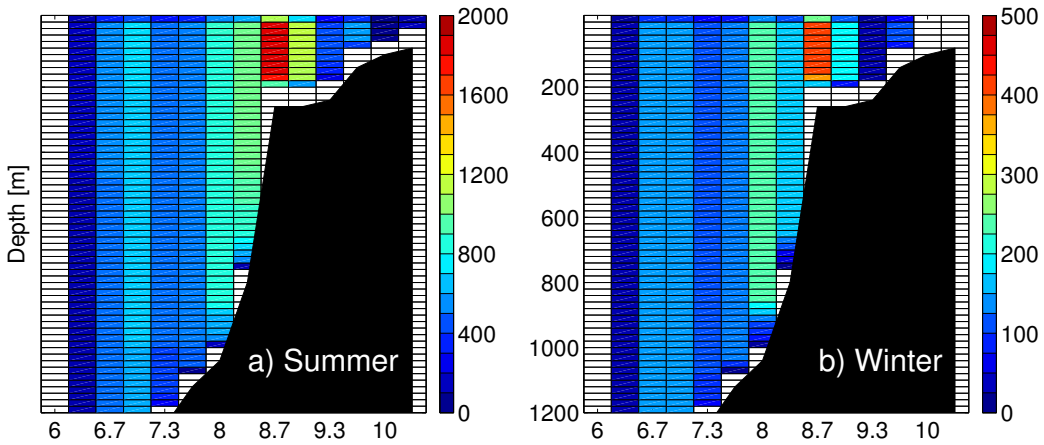

Figure 2.3: Distribution of samples per grid point in depth. Note the difference in color scale between the two plots. The bathymetry is lowered approximately 60 m to not cover the deep grid close to the upper slope (7.66 to 8.33°E. Note the difference in color scale between summer and winter (a and b respectively).

them are done using Nansen bottles, and not a CTD. To prevent misrepresentations caused by this low resolution missing data is linearly interpolated before calculating a mean. Another problem is due to the shelf's irregular bathymetry. When a profile is much deeper than the grid center the data points below the grid centers depth is removed. This may cause an unproportioned profile with a too deep surface layer which may influence the location of the shape of the surface layer. It is important to be aware of both these problems when inspecting the resulting climatological hydrographic sections. In Figure 2.3 the distribution of samples per grid point in the vertical is presented (note the difference in scale between summer and winter). To be able to distinguish the bins, each box represents a sum of samples every 20 meters. Thus, the exact number of samples is not expressed per depth, but it serves as a comparison between grid boxes and gives an overview of the density distribution of sampled data points.

Profile distribution per year per season from 1956 to 2013 is presented in Figure 2.4a. As seen there is not much data before the mid 80s, and especially during winter. From the late 1990s the data availability increases almost exponentially during summer. For winter most of the data is from the first decade of the 2000's. The monthly distribution is presented in Figure 2.4b and shows that all the winter data is collected from the last part of the Arctic winter, April and May. Data density is increasing through the summer, with a peak in September, the second last month in the summer period. The main body of the data is collected along the chosen grid latitude (78.83°N) as seen in Figure 2.4c, both for the summer and winter period. Hydrographic stations are collected from the whole grid during summer, but the winter profiles are largely found in the proximity of the grid center (See also Figure 2.1).

Climatological periods

A climatology is a long time average, normally 30 years or more. In this work the temporal boundary is from 1956 to 2013, but in practice the time series starts in 1986 for summer and 1997 for winter. The months chosen for summer are June, July, August,

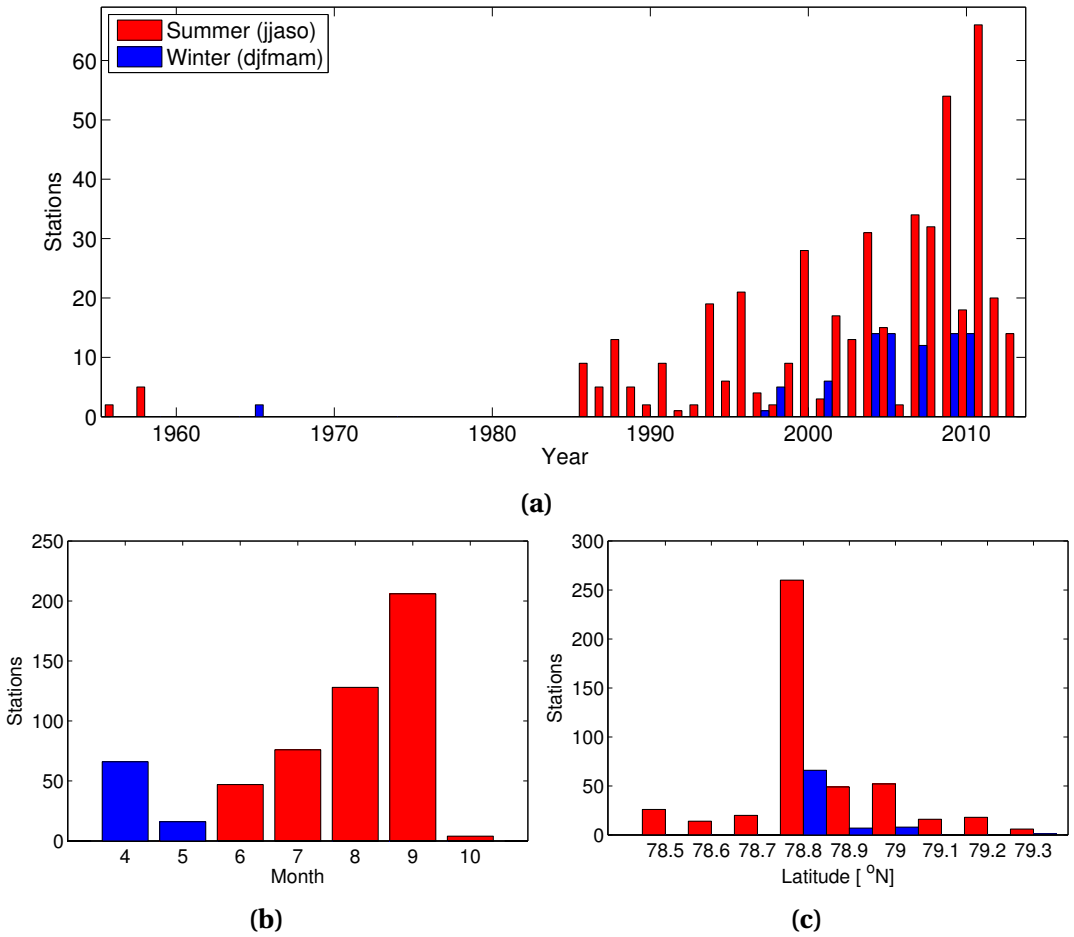

Figure 2.4: Temporal and spatial distribution of the CTD profiles used to construct the summer and winter climatology.

September, and October, while the winter months are December, January, February, March, April, and May. Due to this only the three sections calculated from either the total data or a complete seasonal dataset (summer/winter) is referred to as climatologies. The three sub-periods chosen are referred to as anomaly periods. In the late 1990s, and mid 2000s the WSC experienced two warm anomalies observed in several independent time series (Polyakov et al., 2005; Beszczynska-Möller et al., 2012). The latter of these anomalies can be observed in the right panel of Figure 1.3. Thus, the data set used here is divided into three anomaly periods to identify this event. The first period is from 1956 to 2003, the second period from 2004 to 2007, and the third is from 2008 to 2013. The data availability for the three periods for summer and winter is seen in Table 2.2. Each column in Table 2.2 represents one bin, and each row one period. The rightmost column shows the total number of stations used per section.

Statistical method

Arithmetic mean

As seen in Section 2.2 (Figure 2.2) the number of CTD profiles used per grid point when calculating the climatology is small during winter. The summer climatology is expected to be more robust as it contains more than four times as many profiles. Even so, the large body of the grid points contains less than or close to 30 profiles (N <

Table 2.2: Overview of data availability for the three climatological periods for both summer and winter, for the total data set see Figure 2.2. The three periods are from 1956 to and including 2003, 2004 to and including 2007, and 2008 to and including 2013. Each number represent the number of stations used to calculate the mean profiles for each of the three climatological periods.

Period	6 to 6.7°E			7 to 7.7°E			8 to 8.7°E			9 to 9.7°E			10 to 10.3°E		Total
							Summer								
1st	0	6	5	15	8	10	17	18	34	23	18	13	1	7	175
2nd	0	1	5	6	4	3	7	12	24	12	4	4	0	0	82
3rd	0	1	16	17	14	16	21	23	41	32	9	13	1	0	204
							Winter								
1st	0	0	3	0	1	2	1	4	1	1	1	0	0	0	14
2nd	0	1	2	3	3	3	6	3	11	5	0	3	0	0	40
3rd	0	0	2	4	1	1	4	2	8	4	0	2	0	0	28

30 where N is number of samples). For consistency an unbiased sample variance (s^2) estimator is used when calculating the sample standard deviation. The unbiased sample variance is calculated from

$$s^2 = \frac{1}{N-1}\sum_{i=1}^{N}(x_i - \bar{x})^2, \tag{2.7}$$

where $\bar{x}$ is the mean and x_i is the sampled data point. The unbiased sample standard deviation is given as $s = \sqrt{s^2}$.

Propagation of error

Consider a function $F(x, y, z)$ with error s_F, and where the errors of x, y, and z are given as s_x, s_y, and s_z respectively. s_F is based solely on the errors of its variables, and can be calculated using the variance formula given as

$$s_F^2 = \left(\frac{\partial F}{\partial x}\right)^2 s_x^2 + \left(\frac{\partial F}{\partial y}\right)^2 s_y^2 + \left(\frac{\partial F}{\partial z}\right)^2 s_z^2. \tag{2.8}$$

To find the error of a density field calculated from salinity and temperature, $\rho(S, T)$, (2.8) is simplified to

$$s_\rho^2 = \left(\frac{\partial \rho}{\partial S}\right)^2 s_S^2 + \left(\frac{\partial \rho}{\partial T}\right)^2 s_T^2 \tag{2.9}$$

where s_S and s_T are the standard deviations of their respective parameters. As the Equation of state of seawater is very complex it is difficult to calculate derivative needed for (2.9). To simplify this a linearized Equation of state which yield

$$\rho(S, T) = \rho_0\left[1 + \beta_S(S - S_0) - \alpha_T(T - T_0)\right] \tag{2.10}$$

is used. The two derivatives can now easy be calculated to be $\partial\rho/\partial S = \rho_0\beta_S$ and $\partial\rho/\partial T = -\rho_0\alpha_T$. In (2.10), β_S is the haline contraction coefficient, α_S is the thermal expansion coefficient, and S_0 and T_0 are reference values for salinity and temperature respectively.

Table 2.3: Examples of β_S and α_T based on reference values S_0 and T_0. The parameters are used used in (2.10).

S_0	=	35.0 psu	T_0	=	2 °C
β_S	=	7.80×10^{-4} psu^{-1}	α_T	=	7.79×10^{-5} K^{-1}

Smoothing of profiles
After calculating the mean profiles they were smoothed with a running average both vertically and horizontally. This is done to remove smaller spikes and smaller features to have a clearer end product. Even though physical features may be manipulated to some extent the goal is to present a large scale climatological view of the WSC. For instance a small, warm water intrusion into colder water will not be visible in the final result. It will, however, contribute to increase the temperature in the whole area where it is observed. The averaged profiles are smoothened vertically with a running average over 50 m when the water column is deeper than 500 m. Profiles shallower than this are smoothed with a box size equal to 1/10th of the columns depth. The latter includes all profiles east of the shelf break.

Standard deviations in the hydrography
The variability founded from standard deviations in temperature and salinity are commented here. The upper 100 m of all sections have generally standard deviations for density exceeding 0.2 kg m^{-3}. This is expected as the surface layer is subject to significant external forcing like wind, periodic sea ice drift and atmospheric radiation. The standard deviations for density are highest close to the shelf break and over the WSS, especially during summer. Below the surface layer the variability is smaller, and generally close to 0.1 kg m^{-3}. While this is a large number when taking the density range into account, it does not necessarily mean unreliable data, but rather imply a prominent inter annual variability.

Water masses of the West Spitsbergen Current

When the two branches of the Norwegian Atlantic Current (NwAC) converge in FS north of 76°N, they are subjects to atmospheric cooling and mixing forced by both the atmosphere, ice, and adjacent water masses. These processes alter the properties of the initial water mass and new water masses are formed. Table 2.4 gives an overview of the different main water masses present in the Fram Strait. The definitions are slightly altered from Swift (1986) to easier compare with later work done one the AWI mooring array by i.e. Fahrbach et al. (2001), Schauer et al. (2008), and Beszczynska-Möller et al. (2012).

Originating from the NwAC, the Atlantic Water (AW) is defined as T ≥ 2 °C and $S \geq$ 35 psu. AW is flowing north and loosing heat to both atmosphere and ice melt. The latter is transformed into Arctic Surface Water (ASW). If the AW is kept from being diluted by fresh water, but only loose heat to the atmosphere Lower Arctic Intermediate Water (LAIW) is formed. AW subject to strong cooling and some fresh water input from i.e. ice melt forms Upper Arctic Intermediate Water (UAIW) (Swift and Aagaard, 1981; Swift, 1986). Figure 2.5 shows a T-S plot of all sampling points used to calculate the climatological mean. It is seen that the main body of samples is within the

Table 2.4: Main water masses of the WSC (Swift, 1986; Beszczynska-Möller et al., 2012).

Name		T [°C]	S [psu]
Atlantic Water	AW	> 2	> 34.9
Lower Intermediate AW	LIAW	0 to 2	> 34.9
Upper Arctic Int. Water	UAIW	-2 to 2	34.7 to 34.9
Arctic Surface Water	ASW	> -2	34.4 to 34.8

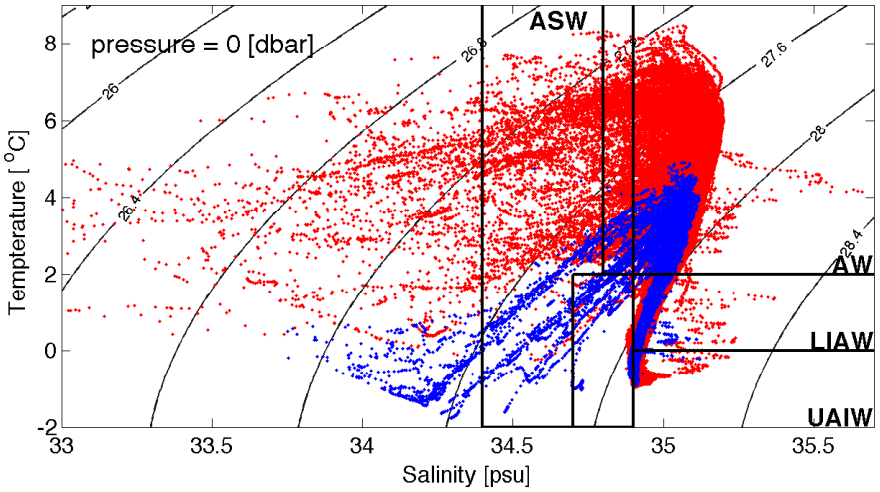

Figure 2.5: T-S plot of all sampling points used to calculate the climatological mean. In total there are 2.3×10^6 points for summer (red), and 0.4×10^6 points for winter (blue). The main water masses are defined in Table 2.4.

four water masses defined in Table 2.4. Red values are from the summer period, and blue are winter values. Due to the nonlinear nature of density as a function of temperature and salinity the linear equation of state, (2.10), is fitted as close as possible in the temperature range of 0 and 6 °C, and salinity range of 34.5 and 35.1 psu. This range is where most of the sampling points are represented. Most of the data points are within the range of AW and ASW for both summer and winter. In addition, the winter period has a significant part of sampling points defined as UAIW. The points with $S \leq 34.4$ psu are mostly found in the upper 50 m of all profiles.

2.3 Current meter data

The data from the current meters was kindly provided by Wilken-Jon von Appen (Personal communication, 2014) at the Alfred Wegener Institute (AWI). An approximation to the barotropic part, v_s^c, of the geostrophic current can be done by calculating a depth mean velocity over a water column. To approximate the barotropic part of the WSC between 6 and 9°E (~ 24 km) in-situ current meter data from the AWI mooring array along 78.83°N was used (Fahrbach et al., 2001). The current meter time series used for this work starts in December 1997 and ends in May 2012 with data from November removed for consistency with the hydrography. As seen in Figure 1.2 the

Table 2.5: Table with position and depth of the current meters used. The 750 m instruments were added summer 2002 (except for F2 where it is the bottom instrument), F5's 750 m instrument was added summer 2003. Note that the standard depths may vary with as much as 200 m due to highly irregular bathymetry and vertical mooring motion. The along slope velocity and north-south current are seen below the double line. *Only data from September 2007 to June 2008.

	F5	F4	F3	F2	F1	F0*
Lat [°N]	78.8329	78.8337	78.8338	78.8342	78.8343	78.8348
Lon [°E]	6.0003	6.9973	8.0005	8.3293	8.6743	8.8637
Mooring depth [m]	2415	1429	1010	779	229	224
Instrument depth						
50 m	×	×	×	×	×	×
250 m	×	×	×	×		
750 m	×	×	×			
1500 m	×					
10 m above sea floor	×	×	×	×	×	×
Along slope direction [m s^{-1}]	0.0480	0.0737	0.1056	0.1698	0.2128	N/A
North-south direction [m s^{-1}]	0.0465	0.0669	0.1045	0.1638	0.2001	0.1087

mooring array covers all main water layers in the water column from 10 m above sea floor to 50 m below sea surface. The original moorings are named F1 to F14 from west to east, and the two extra moorings deployed in 2002 are named F15 and F16 from west to east. From September 2007 to September 2009 an additional mooring, F0, was deployed on the West Spitsbergen Shelf Break by the International Polar Year (IPY) project Integrated Arctic Ocean Observation System (iAOOS) Norway (Teigen et al., 2010). In this work the data from September 2007 to June 2008 is used from F0. An overview of the moorings used to calculate approximations to v_s^c of the WSC is seen in Table 2.5 where the available depths are marked with an ×. It is important to note that the calculated v_s^c is sensitive to instrument failure, especially if the surface layer instruments fails. As the surface layer instrument have significantly higher velocities compared to the current meters deeper down, a long time failure will give a to low velocity for that specific average.

The procedure for calculating the depth averaged velocity for the current meters in moorings F1 to F5 is outlined in the following. First the depth mean current direction is calculated for each mooring. Secondly, the velocities are rotated according to the mean current direction which is different for each mooring. Then the depth mean is calculated for all time steps for each mooring, and a lowpass filter with a cut-off frequency of 7 days is applied. The filter is used to remove wind and tidal variability. Finally the velocities are rotated back with northward and eastward as positive direction to be consistent with velocities calculated from altimetry and hydrography. Furthermore, v_s^c is calculated for each of the three anomaly periods, and used for calculating the anomaly periods geostrophic velocity. This produces lower v_s^c compared to the rotated along current velocity, but the difference is typically less than 0.01 m s^{-1} as seen below the double line in Table 2.5. For the current meters on mooring F0, v_s^c was obtained by first calculating the depth average for each time step. Afterwards, the temporal average was calculated for each season. The fact that the data was not

filtered and have a significantly shorter time series makes the v_s^c calculated for F0 is less reliable with respect the v_s^c obtained from F1-F5. Due to this, v_s^c from F0 is only used for reference for the skewed barotropic jet expected (Fahrbach et al., 2001; Teigen et al., 2010).

2.4 Altimetry

To accurately describe ocean currents by using altimetry, two key parameters are measured, the Geoid and the Sea Surface Hight (SSH). It is also necessary to define a reference level for these two parameters, the reference ellipsoid of the earth. A schematic of the Geoid–SSH system is displayed in Figure 2.6.

The SSH is the distance from the reference ellipsoid to the measured sea surface at a specific point both spatial and temporal. The measurements are done using radar waves emitted with frequencies that penetrate the atmosphere with little distortion, and that are reflected by the ocean. As the wave travels with a known speed (c_0) the distance between the ocean and the satellite can be calculated by measuring the time the the wave uses from its source and back. Even though the principle is simple, very complex post processing in needed to account for the non-homogenous atmosphere. Additionally the satellite orbit must be known with high accuracy. The tides and skewed shape of waves must also be accounted for (Sanford et al., 2011). The SSH is divided into two components, the Sea Level Anomaly (SLA) which varies with time, and the Mean Sea Surface (MSS) which is the mean state of the ocean. The

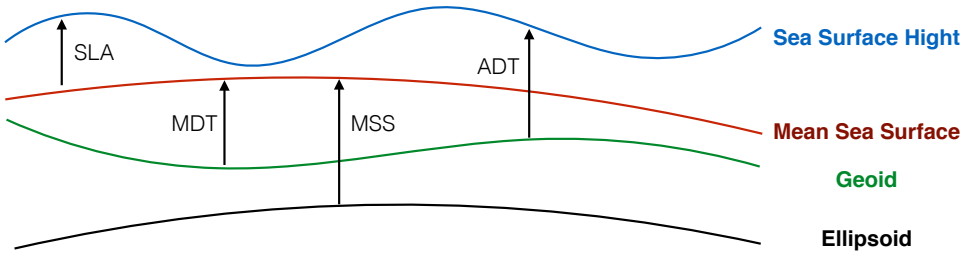

Figure 2.6: Schematic of the Geoid, Ellipsoid, Mean Sea Surface, and Sea Surface Hight. Calculated parameters are also included (ADT, MDT, MSS, SLA).

SLA used is prepared by Ssalto/Ducas (Segment Sol multimissions dÁLTimétrie, dÓrbitographie et de localisation précise/Data Unification and Altimeter Combination System) and supported by Centre National d'etudes spatiales (CNES). The MSS is the MSS_CNES_CLS2011 from Collecte Localisation Satellites Space Oceanography Division. Both data sets are distributed by AVISO (AVISO, 2014; *AVISO Products* 2014).

The Geoid is a mathematical representation of the earth and represents the equipotential surface of the earth's gravity field. This surface coincides with the ocean surface if the atmosphere and tides are removed. Density variations of the solid earth and the atmosphere are problems related to the calculation of the Geoid. The time dependent variation between the Geoid and the SSH is called the Absolute Dynamic

Topography (ADT), and is calculated from

$$\text{ADT} = \text{MSS} + \text{SLA} - \text{Geoid}. \tag{2.11}$$

This makes the ADT the ocean's deviation from the equilibrium state of the Geoid, hence it induces a pressure driven surface velocity. It is important that the Geoid is calculated with reference to the same reference ellipsoid as the MSS/SLA. The EIGEN 6C2 is model used to calculate the Geoid used in this work (available from ICGEM Potsdam: http://icgem.gfz-potsdam.de). The DTU10 (Technical University of Denmark) global ocean tide model is used together with data from the satellite missions LAGEOS-1 and -2, GRACE and GOCE was used to develop the model. These satellites used to obtain both the MSS/SLA and Geoid are briefly described in the following.

SSH satellites

The satellites used to calculate the SSH used in this work are listed in the following.

ERS-1/2

European Remote-Sensing Satellite 1 and 2 was launched into a sun synchronous orbit in 1991 and 1995, and ending in 2000 and 2011 respectively. The orbit perigee was 780 km, and had a period of 100 min with a 24 h delay between them. The mission was funded by ESA (AVISO, 2014; ESA, 2014a).

TOPEX/Poseidon-1/-2

Funded by CNES and NASA the TOPEX/Poseidon mission lasted from 1992 until 2006. The mission used two different sensors to measure the sea surface. NASAs TOPEX sent microwaves with frequencies of 5.3 and 13.6 GHz. The CNES Poseidon 1 was a prototype sensor sending 10% of the time at 13.65 GHz and verified against the TOPEX data set (AVISO, 2014; NASA, 2014a).

GFO

A NASA mission named GeoSat Follow-On started in 1998, and was terminated in 2008 due to decay. The perigee of the satellite was 800 km and it had a period of 100 min. Its main mission was to determine the SSH, and used a radar altimeter measuring at 13.5 GHz (AVISO, 2014).

ENVISAT

With a perigee between 780 and 800 km, ESAs Environmental Satellite was active between 20022012. The period of the satellite was 100 min. An enhanced Radar Altmimeter 2 (RA-2) was measuring on both 5.3 and 13.6 GHz (AVISO, 2014; ESA, 2014a).

Jason-1/2

Jason-1 and -2 was launched as a collaboration between NASA and CNES in 2001 and 2008 respectively. The satellites perigee is 1336 km, and it measures the same point of the earth every 5 days. The two satellites use the Poseidon-2 and -3 respectively to measure SSH with microwaves. Jason-1 was decommissioned in July 2013, but Jason-2 is still operating (AVISO, 2014; NASA, 2014a).

CryoSat-2
An ESA mission launched in 2010 with a perigee of 717 km, and is specifically designed to cover the polar regions. CryoSat-2 has a polar orbit with an inclination of 92°. The Synthetic Aperature Radar/Interferometric Radar Altimeter (SAR/Siral) is able to measure both SSH and sea ice parameters (AVISO, 2014; ESA, 2014a).

Gravity satellites

The gravity satellites used to derive the Geoid model used in this work are listed in the follwing.

LAGEOS-1 and -2
LAser GEOdynamics Satellites (LAGEOS)-1 was designed by NASA, and first launched in 1976. In 1992 the Italian Space Agency designed LAGEOS-2 on the basis of LAGEOS-1 with support from NASA. The satellites are spherical aluminum bodies with a diameter of 0.6 m weighting just above 400 kg. The surfaces are covered of 426 corner reflectors reflecting laser beams sent from fixed positions on the earth. The two satellites very stable orbits makes it possible to determine position with high accuracy. Orbit perigee is 5860 and 5620 km, and the period around the earth is 225 and 223 min for LAEGOS-1 and -2 respectively (ILRS, 2014).

GRACE
The Gravity Recovery and Climate Experiment (GRACE) was launched in March 2002 as a joint collaboration between NASA and the German Aerospace Centre. The goal of the program was to improve and increase the quality of the measurements of earths gravitational field. The mission consists of two identical satellites traveling with a polar orbit and perigee of500 km above the earths surface. Traveling with a distance 220 km between them they can measure the change in distance when the first of the satellites accelerates due to change in gravity. The precision of the distance measurement is 10 µm (NASA, 2014b).

GOCE
Gravity Field and Steady-State Ocean Circulation Explorer is a satellite funded by the European Space Agency (ESA), and launched in March 2009. It crashed on 11 November, 2013 after running out of propellant. The satellite has a significantly lower perigee of 260 km compared to GRACE and LAGEOS-1 and -2. This low orbit allowed for much higher quality of the measurements, as well as the instrument it self, an Electrostatic Gravity Gradiometer, is about 100 times more accurate than any other accelerometers at the time of construction (ESA, 2014b).

CHAPTER 3

RESULTS

3.1 Climatology

Here, the results of the hydrographic CTD sections calculated along 78.83°N between 6 and 10.3°N are presented. First the total climatology calculated from the full data set is presented, secondly the separate summer and winter period is presented, and finally summer and winter sections for the three anomaly periods 1956 to 2003, 2004 to 2007, and 2008 to 2013 are shown. To make comparison between all the CTD sections easier they are plotted with the same contours. Furthermore, it should be kept in mind that the upper 8 m of all stations collected have been removed due to very unevenly data distribution close to the surface, and the minimum values for salinity and density are set to 34.5 psu and 27.5 kg m^{-3}.

The full climatological sections for temperature, salinity and density are presented in Figure 3.1. Temperature is shown in Figure 3.1a. West of the shelf break the upper 50 to 150 m have temperatures above 5 °C. This layer is shallower furthest west, and deepens towards the shore. Two small patches with temperatures above 5.5 °C in the upper 50 m at 6.3°E and between 7 and 7.7°E. Temperatures below the surface layer decrease with depth to below −0.5 °C at 1000 m. The horizontal temperature gradient is varying, but is in general positive west of the shelf. The strongest gradient is found at 100 to 600 m between 7.7 and 8°E. Over the WSS the water has temperatures exceeding 2 °C and most of the shelf have water warmer than 3°E. The coldest water is found furthest to the east. An intrusion of water warmer than 3 °C is seen over the shallow part of the shelf between 50 to 100 m depth. A small spike with T > 4 °C related to this intrusion.

Figures 3.1b shows the salinity section. A fresher surface layer is seen which deepens from 30 to 100 m along the whole section. The salinity is above 34.9 psu below this layer for the whole section including the shelf. A core of water with salinity above 35 psu is seen from below the surface layer and down to approximately 500 m. The bottom boundary of the 35 psu contours have some irregularities, and is deepest close to the slope at 8.3°E.

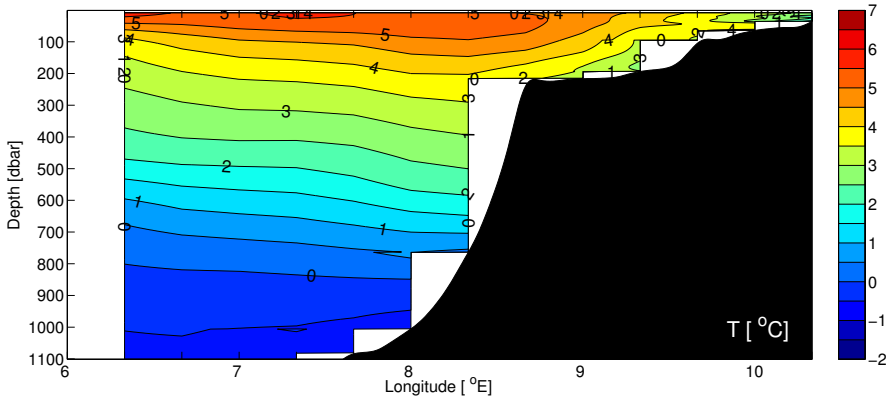

(a)

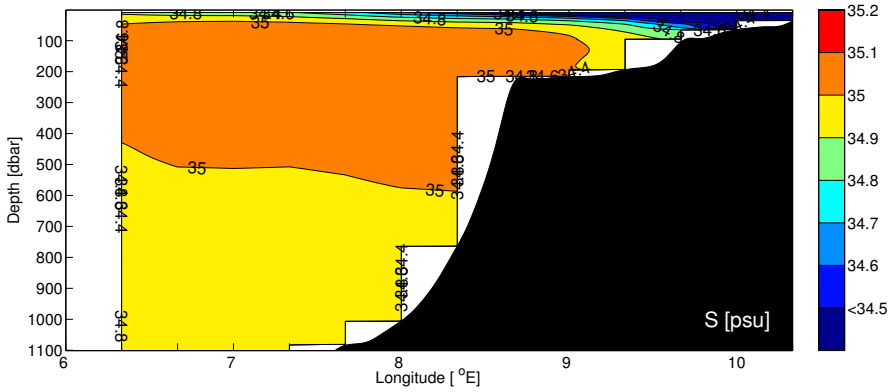

(b)

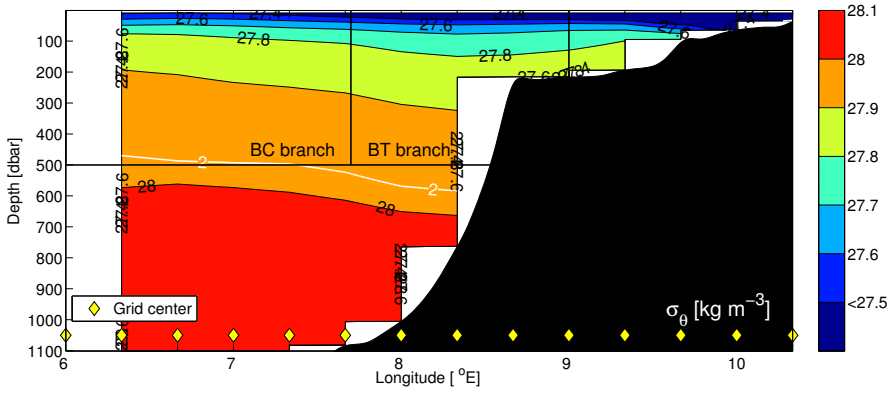

(c)

Figure 3.1: Total climatology calculated from all data availible. a, b, and c show temperature, salinity, and density respectively. The reference pressure is set to 0 dbar. In (c) the white contour line in is the 2 °C contour line, and the yellow diamonds represent each centered grid point.

Density is presented in Figure 3.1c. Over the upper shelf and deep water the horizontal density gradients are generally negative but with some irregularities. The strongest gradients are found in the same area as the strongest temperature grandients, from 100 to 600 m between 7.7 and 8°E. Over the shelf the horizontal gradients turn positive between the shelf break and 9.3°E, before again turning negative east of 9.3°E. To give an impression on where the core of Atlantic type water is located the white contour line shows the T = 2 °C contour. This is done for all CTD sections.

Summer (jjaso)

Figure 3.2 show the summer climatology for temperature, salinity and density respectively. The temperature is seen to have its maximum, warmer than 6 °C, in the upper 50 meter layer west of the WSS in Figure 3.2a. Further down in the water column, west of the WSS, the temperature is seen to decrease close to linearly to a temperature minimum below 1000 m depth. A positive horizontal temperature gradient is seen in the upper 400 m west of 7°E. A similar positive gradient is found below the temperature maximum and down to 750 m from 7.5°E towards the West Spitsbergen Continental Slope (WSCS). Moving onto the WSS the temperature field is not as smooth as over the deeper waters due to few hydrographic profiles available to calculate the average. A negative horizontal temperature gradient can be seen at 8.3°E in the surface layer and continues towards the shore. This horizontal gradient is notably stronger than the gradients seen over deeper water. The vertical temperature gradient over the WSS is also in general positive, but it is not as strong as over the deep water. East of 9.7°E the temperature data appear to be noisy. This is due to the low data availability at 10°E, and the variation in the profiles is distinct. Between 9.3 and 10°E a local temperature maximum spike is seen at about 100 m depth which is stemming from the same problem with low data coverage. The maximum temperature in the section is 6.22 °C at 7°E.

The salinity for the summer period is seen in Figure 3.2b. Minimum salinity is found in the surface layer which is shown only in the upper 20 to 50 m over the deep and water upper slope. The low salinity layer deepens over the slope towards the east, and east of 9.7°E salinity is below 34.5 psu for the whole profiles. Approximately between 100 and 200 m depth and 6.5 and 8.5°E a maximum salinity core with salinity above 35.1 psu is found. Below 500 m the salinity is between 34.9 and 35 psu. In the area over the upper slope the horizontal salinity gradient is globally positive below the maximum salinity core. Some smaller variations in this gradient is seen over different interval, mainly along the 35 psu contour line. Above the salinity core the gradient appears to be equally negative. The upper layer with the salinity minimum deepens towards the shore. Close to the shore the whole water column (h < 100 m) is seen to have salinity less than the minimum value of 34.5 psu. At 100 m depth a spike in the salinity is seen in the 35 psu contour line between 9 and 9.3°E. Over the WSS the global horizontal salinity gradient is negative in all layers, and it increases with depth.

The density field plotted in Figure 3.2c, and its contour lines share many of the same features as the ones of the salinity. The surface layer with a potential density lower than 27.9 $\mathrm{kg\,m^{-3}}$ is mainly above 100 m, but closer to shore the fresh surface layer

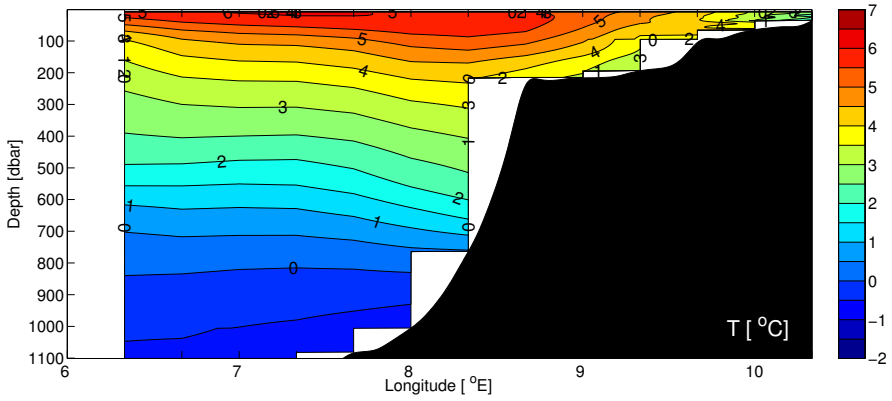

(a)

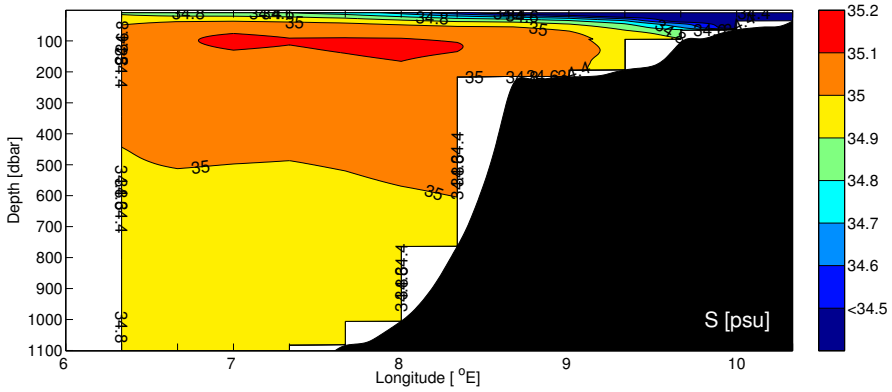

(b)

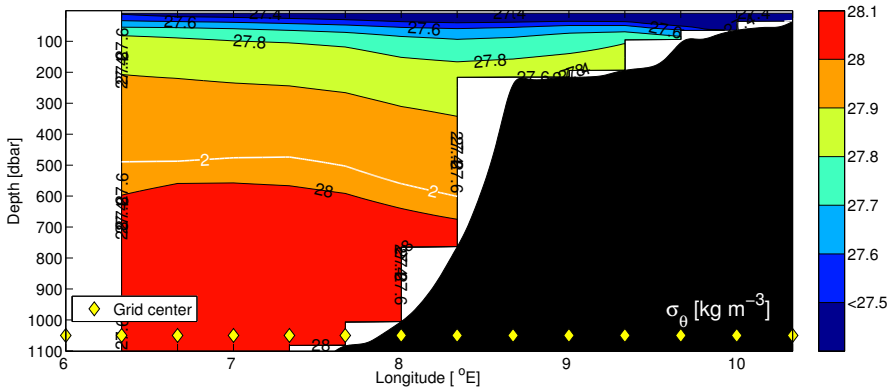

(c)

Figure 3.2: Summer climatology (jjaso). See also caption of Figure 3.1.

deepens down to the bottom. Below this surface layer a negative horizontal density gradient can be seen through the large body of the water mass west of WSS. One exception is the 28 kg m^{-3} contour from 6.3 to 6.7°E where it is slightly positive. Over the shelf the density gradient is again positive from the shelf break until 9.3°E, or about 200 m depth.

Winter (djfmam)

The winter climatology is presented in the right column of Figure 3.3 in the same way as summer (temperature, salinity, and density respectively). In Figure 3.3a it is shown that the temperature maximum is deeper down in the water column compared with summer. The small oval core of warmer than 3.5 °C water is seen between 60 and 200 m depth and 7 to 7.7°E. The maximum temperature in the core is 3.69 °C at about 80 m. Water temperatures above 3 °C extend over much of the upper 400 m west of the West Spitsbergen Shelf Break with a similar oval shape. However two 'arms' extend out of the core, one westward in the surface, and eastwards towards the shelf break between 150 and 250 m.

Over the slope, below 500 to 600 m, the temperature is gradually decreasing from 2 to 3 °C to less than 0 °C below 800 m, but with a notable positive vertical temperature gradient. At 750 m a positive local temperature maximum is seen at 8°E. At 6.5°E the 3 °C contour line outcrops to the surface. The water temperature decreases from 2.5 °C to less than 0 °C towards the shore. However, from 50 to 120 m an intrusion of higher temperature extends onto the shelf. A similar intrusion of warmer water is evident along the bottom furthest out on the WSS penetrating under the colder water.

Figure 3.3b shows a fresh surface layer from 7°E and continuing shorewards, and along this layer the depth of the fresh layer deepens to below 100 m close to the shore. A core of S ≥ 35 psu covers most of the area below the halocline and down to 500 to 600 m depth. The salinity does not exceed 35 psu over the shelf break, but an intrusion of water with salinity above 34.9 psu is seen below the halocline. Furthest west, close to 6.5°E the 35 psu contour outcrops to the surface. This is the same place as the 3 °C contour outcrops. The horizontal salinity gradient is positive above the shelf break depth, and strongest in the deeper levels over the shelf. The lower limit of the 35 psu contour starts at 400 m over the deeper water, and deepens towards east. It reaches a maximum depth of 650 m at 7.7°E. East of 7.7°E the depth of the contour decreases. Below this line, down to 1100 m, most of the water have a salinity exceeding 34.9 psu, but a fresher patch is seen west of 7°E in the deeper part of the section.

The winter density climatology is shown in Figure 3.3c. Unlike the summer section, the winter section is missing the defined surface layer, and appears more homogenous. The density minimum is found over the shelf with σ_θ = 27.65 kg m^{-3} close to the surface. A small core with density above 27.9 kg m^{-3} is seen over the shelf between 9 and 9.3°E. This core is not directly connected to the 27.9 psu contour line over the shelf, but along the bottom of the shelf between 8.7 and 9°E the density is seen to exceed 27.9 kg m^{-3}. West of the shelf break the horizontal density gradient is close to zero, but further out it have the same concave lower shape as the S = 35 psu contour.

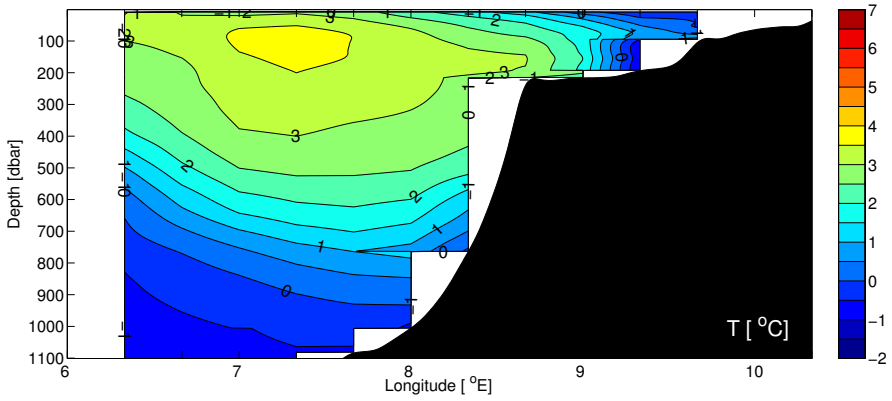

(a)

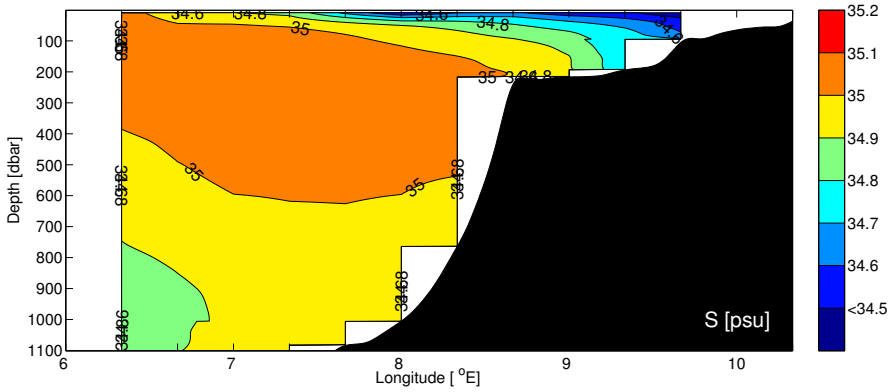

(b)

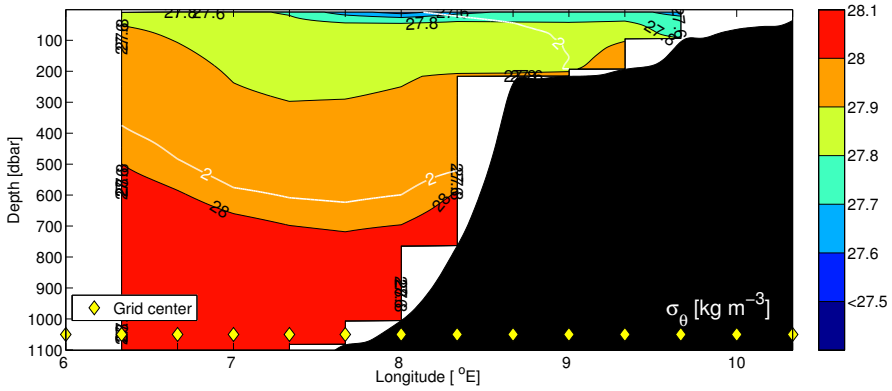

(c)

Figure 3.3: Winter climatolgy (djfmam). See also caption of Figure 3.1.

Anomaly Periods

Now the data set is divided into three climatological periods, the first from 1956 to 2003, the second from 2004 to 2007, and the third from 2008 to 2013. The three periods are chosen to identify the warm anomaly detected in the FS in the mid 2000s. In addition, this give one period before and one after the anomaly period. An overview of the data available for these three periods was presented in Section 2.2, Table 2.2.

First Period (1956-2003)
The summer data is presented in Figure 3.4's left column. Temperature maximum in Figure 3.4a is close to the surface, with temperatures above 5 °C in the upper 100 m over the deep water and slope. Above 500 m the water has temperatures above 2 °C. Below 500 m the temperature decreases to a minimum of about −0.5 °C. The horizontal temperature gradient is positive between 6.7 and 8.7°E, and slightly negative west of this. Over the shelf the temperature decreases eastwards to less than 2 °C. From 9.7°E and eastwards the temperature field appears noisy due to the lack of data. Figure 3.4c shows the first periods salinity section for summer. A fresh surface layer in seen down to about 50 m east of 7°E and deepening gradually to 100 m over the shelf. From 100 to 500 m a core with S ≥ 35 psu is positioned over the slope, with a small intrusion onto the shelf at between 100 and 200 m depth. Below the 35 psu core the salinity in between 34.9 and 35 psu. The density field calculated from the above temperature and salinity is presented in Figure 3.4e. Furthest west the horizontal density gradient is positive, but turns negative from 6.7°E and towards 8°E. From this point no gradient is seen below 100 m between 8°E and the shelf break. Over the shelf the density gradient again turn positive below 100 m.

The winter climatology for the first period consists of very little data. Only 14 profiles conducted between 1956 and 2001 are used to calculate it, as seen in Table 2.2. This causes the following result to be highly questionable. The winter temperature field for the first period is shown in Figure 3.4b. Temperatures below 2 °C dominate the main part of the upper 50 m. Two warm cores are seen, however, at 6.7 and 8.3 m where the surface temperature is warmer than 2.5 and 2 °C for the two locations respectively. Below 100 m depth between 7 and 7.7°E a warm core with T ≥ 3 °C. A small warm water core with temperature above 3 °C is also seen over the shelf break. Below the shelf break the temperature decreases with depth, and a small temperature maximum warmer than 1.5 °C is seen on 800 m at 7.3°E. This maximum causes a wedge of warmer water to penetrate downwards. The fresh surface layer is displaced by higher salinity at the same two locations as the temperature field does at 6.7 and 8.3°E. Over the shelf the horizontal salinity gradient is negative from S ≥ 35 psu towards the east. Vertical salinity gradient are weak in the same area. A salinity core with S ≥ 35 psu is seen from 7 to 9°E and at 200 to 400 m depth. Close to the shelf break however the depth of the core is almost from 100 to 500 m. The rest of the section have salinity between 34.9 and 35 psu. Figure 3.4f displays that the water with the lowest density follow the temperature and salinity contours in the surface. The outcropped temperature and salinity maximas in the surface described above are also seen in the density section. Horizontal density gradients over the deep water are stronger below 100 m compared to summer, and the strongest gradient is found between 6.7 and 7°E at 100

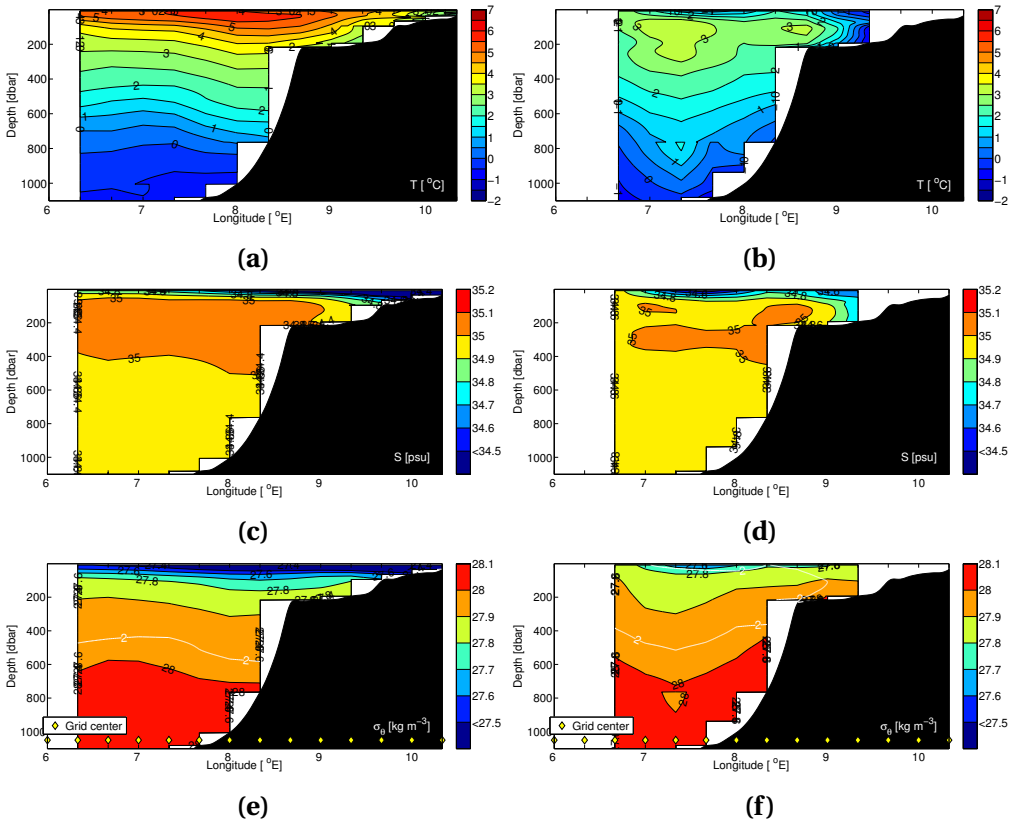

Figure 3.4: Climatology for temperature, salinity and denity during the temperature anomaly between 1956 and 2003. The left column, (a), (c) and, (e), include the summer sections, and the right column, (b), (d) and, (f), show the sections for winter.

to 300 m depth. Over the upper slope the horizontal density gradient is close to zero down to 500 m, but below that depth it turns positive. From the shelf break and eastwards the gradients are in general slightly positive. A patch with low density at 800 m, 7.3°E is seen to correspond to the warm water patch described above.

Second Period (2004-2007)

The second climatological period is presented in Figure 3.5, and this period is covering the warm anomaly of the WSC (Polyakov et al., 2005; Beszczynska-Möller et al., 2012). Displayed in Figure 3.5a is the second period's summer temperature section. A temperature maximum is seen at the surface, with a more or less linear decrease in temperature with depth. This is especially notable over the deeper water and slope, but can also be seen over the outer part of the shelf. Further towards the shore the temperature is seen to decrease as well over the WSS. This is most prominent close to the surface, but is also visible close to the bottom. An intrusion of warmer water at 70 m depth can be seen east of 9°E. The maximum temperature is 7.15 °C, and is found over the deep water. Figure 3.5c shows a salinity maximum core (S > 35 psu) that has approximately the same depth as the full climatology during summer, but it extends longer in both the vertical and in the horizontal. Its deepest part is at the same depth as the shelf break. A spike with salinity larger than 35 psu is seen between 8 and 8.3°E at 250 m depth. It is not physical, but results from the smoothening procedure because salinity values at both 8 and 8.3°E are very close to 35 psu before

smoothening. From the core and downwards, the salinity decreases to below 35 psu at 500 m. The halocline is for the most part above 100 m depth, but is hardly visible west of 8°E due to an outcrop of the 34.9 psu just west of that point. Over the inner parts of the shelf, where the water depth is close to 100 m shallower, the halocline deepens, and fresher water is seen to dominate close to the coast. Above the upper slope and deeper water the horizontal density gradient is slightly negative, with some smaler variations. The horizontal gradient is slightly positive below 100 m over the shelf, and neutral to slightly negative in the surface. The maximum density over the shelf (27.8 kg m^{-3}) is connected to the same contour line over the shelf.

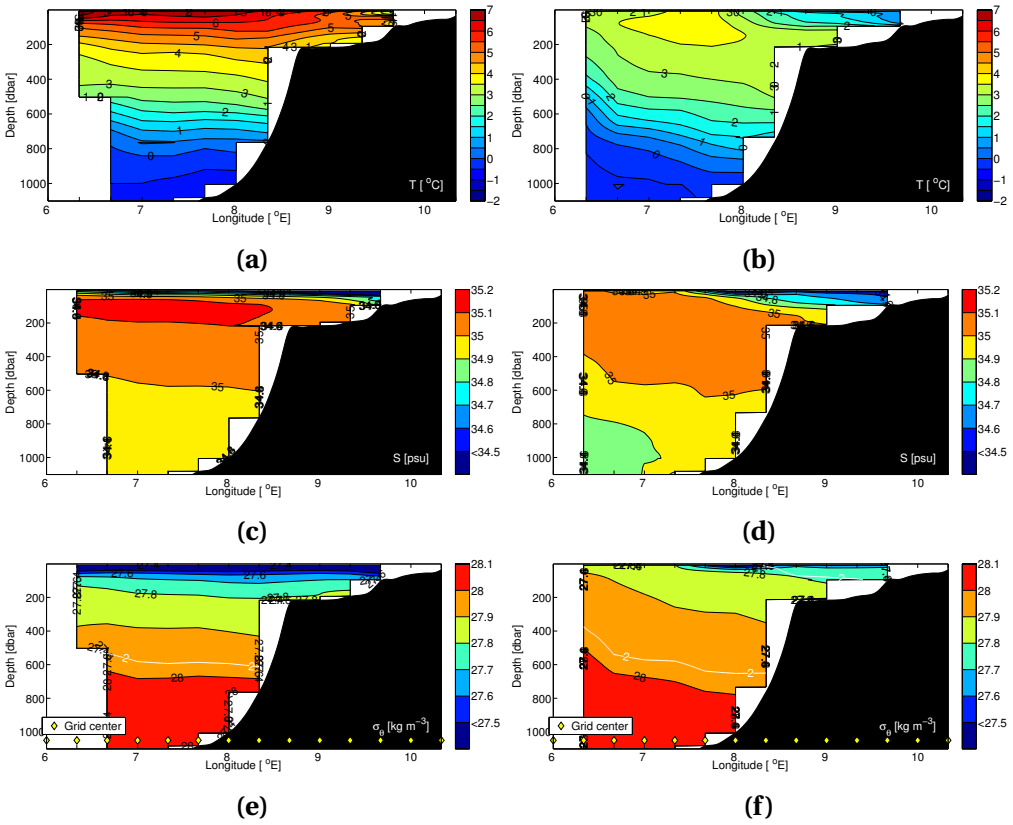

Figure 3.5: Climatology for temperature, salinity and denity during the temperature anomaly between 2004 and 2007. See also caption of Figure 3.4.

Winter climatologies from the second period are presented in the right column in Figure 3.5. The core of water with at temperature higher than 2 °C is found from the surface and down to a maximum of about 650 m over the slope. Further out the core is above 600 m. The oval shape of the warm water core is also evident here, but with an intrusion reaching onto the slope and shelf. West of 8°E the surface temperature exceeds 3 °C, and between7.1 and 8.8°E the surface temperature is above 3.5 °C. Over the shelf the warm water with a temperature above 3 °C dominates the area below 100 m. Above this depth the water is colder, with the coldest water towards the coast. Most of the water west over the shelf is dominated by salinities of 34.9 psu or higher, except from a patch of fresher water below 750 m and west of 7°N. Above 500 m the main body of water has a salinity of 35 psu. No halocline is obvious over the slope, but close to and over the shelf the water is fresher. The water with the lowest salinity is close to the surface furthest east. More saline water is seen onto the shelf below

100 m. The horizontal density gradient is negative, but with varying strength over the whole section. The strongest gradient is found between 6.3 and 7.3°E. East of 7.3°E the gradients are in general decreasing, but they are still notably negative.

Third Period (2008-2013)
The third climatological period from 2008 to 2013 is presented in Figure 3.6. Summer temperature is plotted in Figure 3.6a. It has the typical warm surface with temperature decreasing to below 0 °C below 900 m. In the upper 400 m the horizontal temperature gradient is slightly positive between 6.3 and 8.3°E, and from here it turns negative towards the shallow shelf. Between 400 to 800 m the horizontal temperature gradient is close to zero west of 7.7°E, but turns positive towards the upper slope. Deeper than 800 m the horizontal gradient is positive over the whole area, and the temperature is below 0 °C. Spikes of warm water are visible east of 9.3°E. They are created because some profiles are much deeper than the bathymetry at the grid point, thus only parts of those profiles are used to represent a full water column. Figure 3.6c shows salinity for the third period. A layer with low salinity is seen in the upper 50 to 100 m, deepening over the self. A core with an open border to the west with $S \geq 35.1$ psu is located west of the shelf break below the halocline and at approximately 200 m depth. The high salinity core also outcrops towards the surface at 6.5°E. Below this salinity core the salinity decreases with depth, having a small horizontal salinity gradient. Below the halocline over the shelf the salinity is between 35 and 35.1 psu. The density field presented in Figure 3.6e shows negative density gradients over most of the section below the surface layer. The strength of the gradient are varying, and are strongest between 6.3 and 6.7°E at 100 to 200 m depth, and at 7.7 to 8.3°E between 200 and 700 m. Over the shelf the gradient is slightly positive.

The winter anomaly section for the third period is presented in Figure 3.6. Temperature is seen in 3.6b, and the core of water exceeding 2 °C covers most of the area between the surface and 600 m depth. West of 8°E the surface temperature is seen to exceed 2°E. Below the AW core the temperature decreases to below 0 °C below 800 m. At 750 m three temperature spikes are seen at 7, 7.7 and 8°E. A cold surface layer is seen over the shelf with temperatures below 0 °C east of 9.3°E. The surface salinity exceeds 34.8 psu west of 8°E is seen in Figure 3.6d, corresponding to to the warm surface temperatures described above. Below the surface salinity exceed 34.9 psu with a core between 100 and 600 m and 6.7 and 8.3°E. A small patch of $S < 34.9$ psu is seen at 900 m depth at 6.7°E. East of 9°E the salinity decreases over the shelf towards east, and a negative vertical salinity gradient is seen. Two small spikes in the $S = 35$ psu are seen west of 8°E at 850 m, and east of 8°E at 250 m. A weak negative density gradient is seen in the upper 100 m of the whole density section in Figure 3.6f. Below the surface a negative density gradient is seen from 6.7 to 7.7°E. East of 7.7°E the gradient turns positive towards east. It is seen that the lower boundary of the 35 psu isopycnal follows the 28 kg m^{-3} contour line.

Temperature and salinity of the AW area
The mean temperature of the AW in the three sections is seen in Figure 3.7. Red line represents summer and blue represents winter. The time interval for the first period has been shortened to make comparison to the two shorter time series easier. Figure 3.7a presents salinity data, and it is observed that the salinity is always higher in

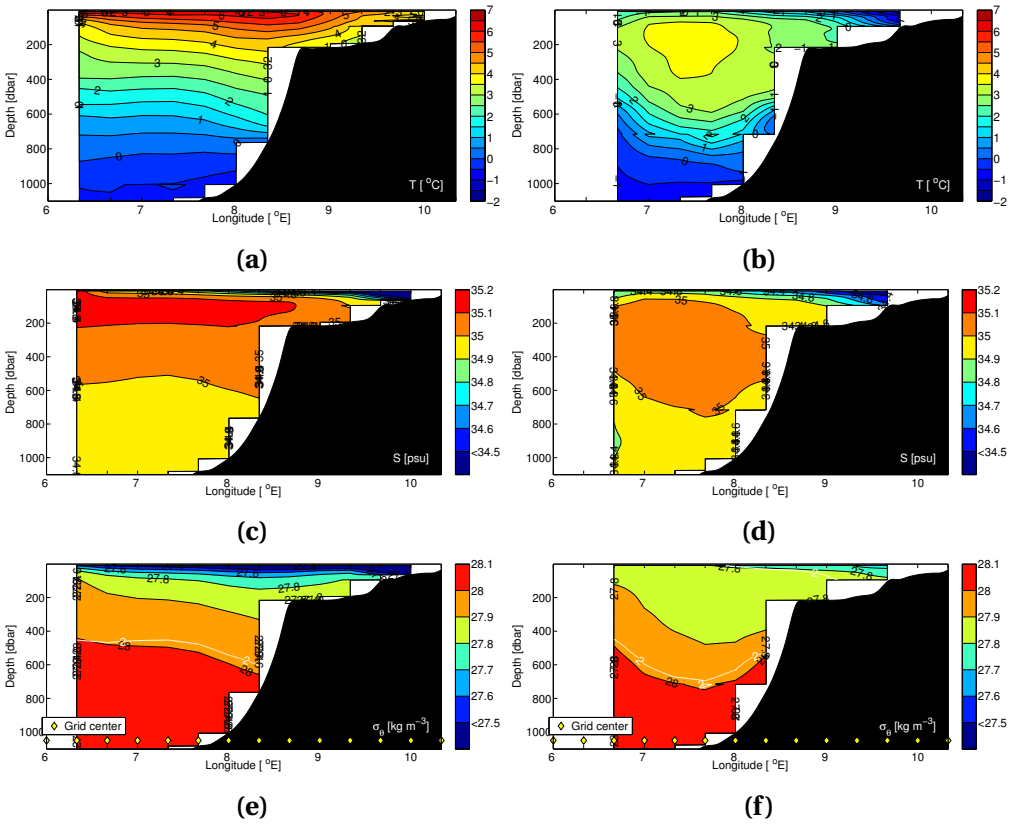

Figure 3.6: Climatology for temperature, salinity and density during the temperature anomaly between 2008 and 2013. See also caption of Figure 3.4.

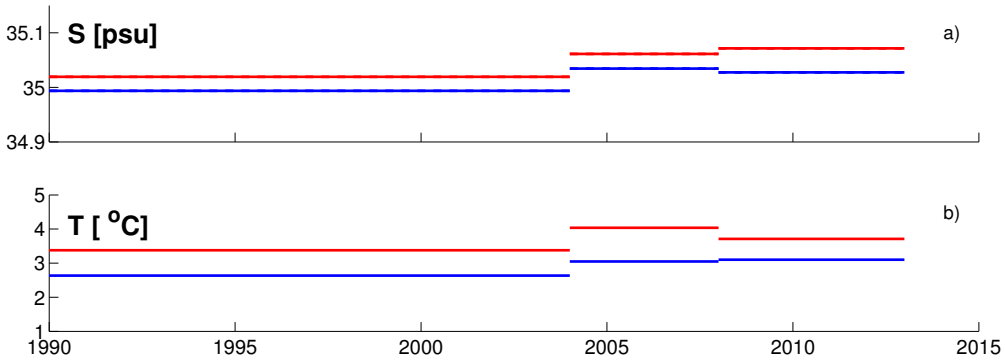

Figure 3.7: Mean temperature of AW in the WSC for the three periods. The data for the first periods extends back to 1956, but the time series is plotted from 1990 to make comparison easier. Red lines are summer , and blue lines are winter data.

summer than winter. For the first period the mean salinities are 35.02 and 35.00 psu for summer and winter respectively. The second period has salinities of 35.06 and 35.03 psu, and the third period has 35.08 and 35.03 psu. The full climatology has a calculated mean salinity of 35.05 and 35.02 psu for summer and winter. Temperature time series is plotted in Figure 3.7b. Mean temperatures for the AW are 3.4 and 2.6 °C for summer and winter respectively for the first period, 4.0 and 3.0 °C for the second period, and 3.7 and 3.1 °C for the third period. The mean temperature calculated from the total climatology are 3.6 and 2.9 °C for summer and winter. Hence the warmest temperature is found in the second period during summer. The winter temperature has a positive trend throughout all three periods.

3.2 Geostrophic velocity

By combining the barotropic and the baroclinic component the geostrophic current can be calculated from (2.2). Two different surface velocities are used, one calculated from the AWI current meters denoted v_s^c, and one calculated from altimetry denoted v_s^a. They are compared in Figure 3.8. Geostrophic velocity sections calculated for summer and winter are presented in Figures 3.9 to 3.13. Sections showing v_g are deeper than the CTD sections in order to show positions of the current meters.

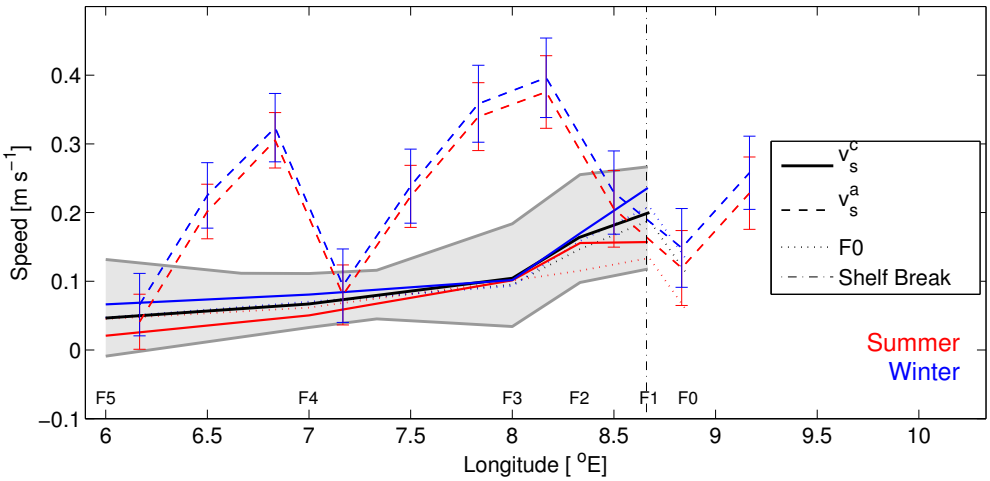

Figure 3.8: Comparison between the two different barotropic velcities v_s^c calculated from the mooring array and v_s^a calculated from the first part on the right hand side in (2.4). The grey shaded area is the boundaries for the yearly mean profiles (W1998-W2012). Solid lines are depth and temporal mean for the whole data set, split in all data (black), summer data (red), and winter data (blue). Dotted lines represent the data between September 2007–July 2008 where F0 also was active. The dashed lines are surface velocities calculated from altimetry.

Surface velocities v_s^a and v_s^c are calculated and plotted from altimetry and current meters for the hydrographical section in Figure 3.8. Red color represents summer data, and blue represent winter. The same v_s profiles are plotted in the upper panels of the v_g sections. The dashed lines represent v_s^a and are calculated from (2.4). They are seen to have a relatively high velocity, and a wave-like structure. Because v_s^a is not

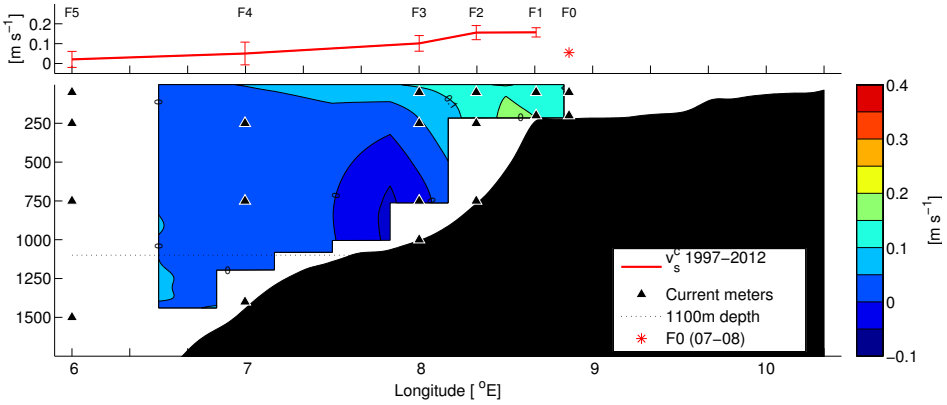

Figure 3.9: Geostrophic velocity for summer (jjaso) calculated from the current meters. The red, solid line is the depth seasonal mean calculated from the moorings F5 to F1, length of dataset used to calculate it is given in legend. The asterix represent seasonal depth mean for the period with F0 data. Black triangles represent the nominal depths of the current meters (may vary with up 200 m depending on deployment), and the dotted line represents 1100 m depth.

trusted over shallow water due to velocities exceeding 0.35 m s^{-1}, and a maximum of 0.72 m s^{-1} east of 10°E, the eastern boundary for v_s^a is set to 9.2°E. Both summer and winter v_s^a have local maximum values at 6.9 and 8.1°E, and minimum values at 6.1, 7.2 and 8.9°E. The global maximum for summer is 0.38 m s^{-1}, and 0.40 m s^{-1}, both at 8°E. The minimum velocities are 0.04 m s^{-1} for summer, and 0.06 m s^{-1} for winter, both at 6°E. The black solid line v_s^c is calculated from all the AWI mooring data between December 1997 and May 2012, while the colored lines are v_s^c for each season to match the hydrographical anomaly periods. The shaded area represents the maximum and minimum seasonal v_s^c calculated at each mooring in the full period. The dotted line represents a data set with moorings F5 to F0 which covers the period September 2007 to July 2008. All the mooring data shows a low, but increasing, velocities over the deep water towards the shelf. Over the upper part of the shelf the velocities increase to a maximum at F1 (0.24 m s^{-1}) for winter, and for both F2 and F1 (0.16 m s^{-1}) for summer. The dotted on-year dataset shows the same trend over the deep water and upper shelf, but at the easternmost mooring (F0) the profile shows a local minimum. In winter the mean velocity at F0 is 0.12 m s^{-1}, and in summer it is 0.05 m s^{-1}.

Current meters (v_g^c)

The geostrophic velocity field, calculated with the data from the mooring array in combination with the hydrographic section, are presented in Figure 3.9 and 3.10 for summer and winter respectively. The positions of the moorings used are indicated in the upper panel. In summer v_s^c has a maximum at the F1 mooring of 0.16 m s^{-1}, and a minimum of 0.02 m s^{-1} at F5. The steady increase over the deep water is from F5's 0.02 to 0.10 m s^{-1} at F3. The seasonal mean velocity for F0 was 0.05 m s^{-1} and is plotted as a red star. The full velocity section presented in the lower panel have maximum velocity, $v_g > 0.24$ m s^{-1}, close to the surface over the upper slope. Towards the bottom the velocity decreases, but the gradients are relatively small over the upper

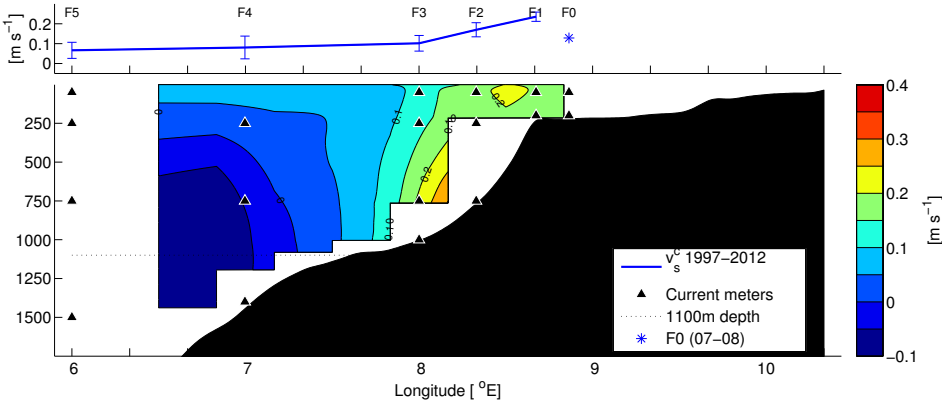

Figure 3.10: Geostrophic velocity for winter (djfmam). See caption of Figure 3.9 for more information.

slope. From the maximum (F3) and horizontally towards the shelf the velocity is also decreasing to below 0.05 m s^{-1}. Unfortunately most of the velocity field east of F3, below the shelf break, is lost due to the used ADT grid. West of F3, the speed decreases below 0.05 m s^{-1}, with small variations over the whole area. The lowest velocities are found west of F4, and in this area the velocities are below 0.01 m s^{-1}.

The v_s^c profile for the winter period is plotted as a solid line in the upper panel of Figure 3.10. Over the deeper water west of F3 v_s^c is lower than 0.10 m s^{-1}. The steady increase for winter from F5 to F3 where it increases from 0.07 to 0.10 m s^{-1} has a weaker gradient compared to summer. East of F3 the velocity increases towards F1 where v_s^c is 0.24 m s^{-1}, the maximum of both the summer and winter profiles. The velocity mean for F0 is 0.13 m s^{-1} and is plotted as a blue star. The lower panel shows two local velocity maxima coinciding with the v_s^c maxima over the shelf break, and a surface intensified current over the deep water between 6.7 and 7°E. The maxima over the deep water decrease with depth, and the velocity is generally less than 0.1 m s^{-1} below 500 m. There is also an area of low velocities between the two maxima. Over the upper slope and shelf break the vertical velocity gradients are very weak all the way from the shelf and out to 8°E.

Altimetry (v_g^a)

Figure 3.11 shows a Hov-Möller diagram of v_s^a along 78.83°N. The dashed lines separate the three anomaly periods, and the dotted line represents the shelf break with depth = 250 m. It is seen that v_s^a at the two local maxima vary between 0.3 and 0.5 m s^{-1}, and v_s^a is always positive. The width of the two current maxima are also changing with time, and the temporal velocity maxima are in general found during winter. The two dash-dotted lines are plotted in the first week of January in 1995 and 1998 respectively to easier see examples of velocity maxima in relation to winter.

Velocity profiles calculated from altimetry and hydrography are plotted in Figure 3.12, and 3.13 for summer and winter respectively. The upper panel in Figure 3.12 shows v_s^a calculated from summer data between 1992 and 2012. The bottom panel present the full geostrophic velocity with depth. It is seen that the maxima in the geostrophic velocity coincide with the maxima of v_s^a. The global maximum velocity

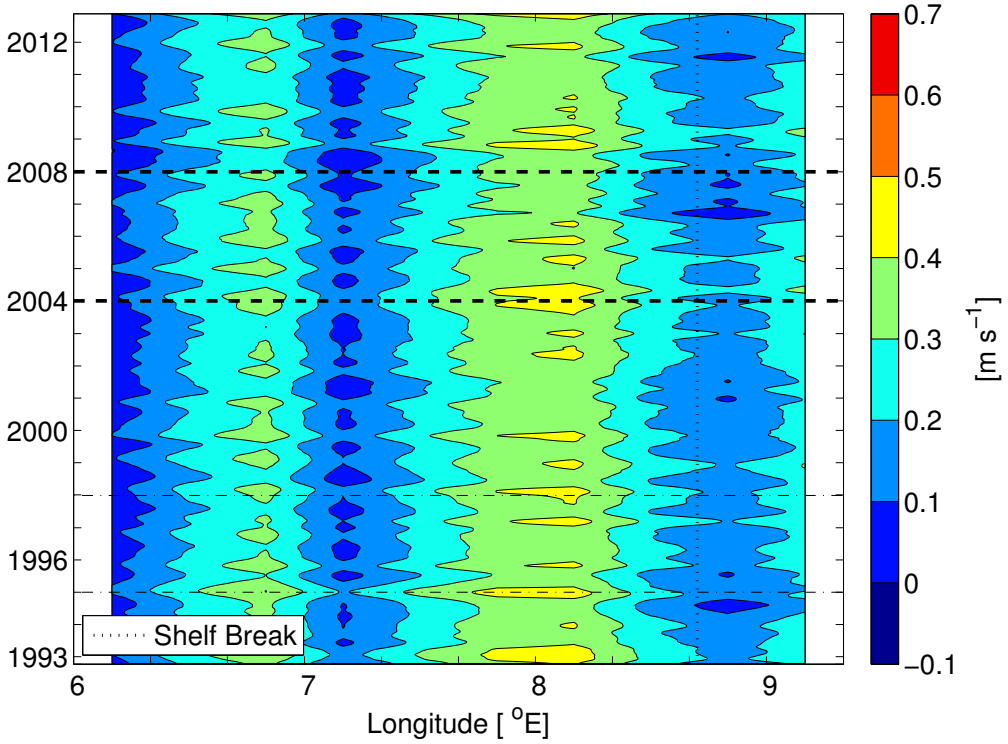

Figure 3.11: Hov-Möller diagram of v_s^a with time on the y-axis and spatial extent on x-axis. The shelf break is marked with a black dotted line. The two dashed lines represent the border between the three anomaly periods.

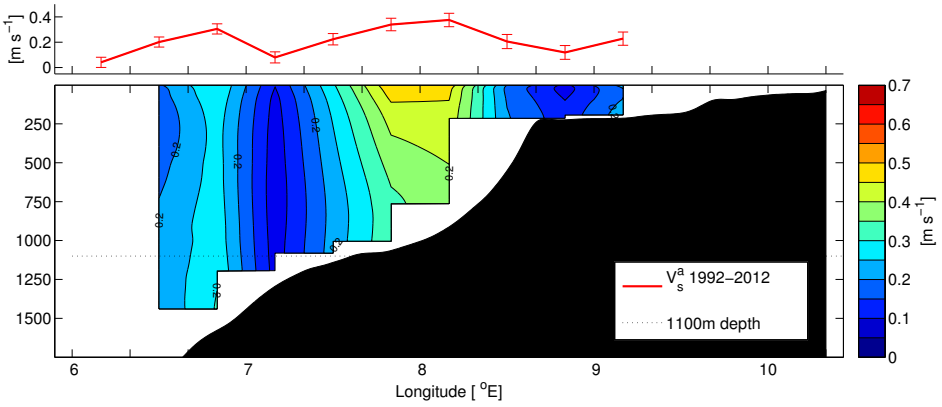

Figure 3.12: Geostrophic velocity for the summer period calculated by using altimetry and hydrography. The upper panel presents v_s^a, and the lower panel presents v_g calculated from (2.4) in all depths. Note that the depth is not consistent with the hydrographic sections (Figure 3.2 and 3.3), but it is with the velocity sections in Figure 3.9 and 3.10.

is 0.49 m s^{-1} and found between 7.7 and 8.3°E in the upper 100 m. Below 200 m the velocity decreases with depth. A local maximum is found just west of 7°E where v_g^a reaches 0.30 m s^{-1} in the surface, below this maxima and down to the bottom v_g^a always exceed 0.25 m s^{-1}. The rest of the section has very small vertical gradients thus being dominated by v_s^a, not hydrography.

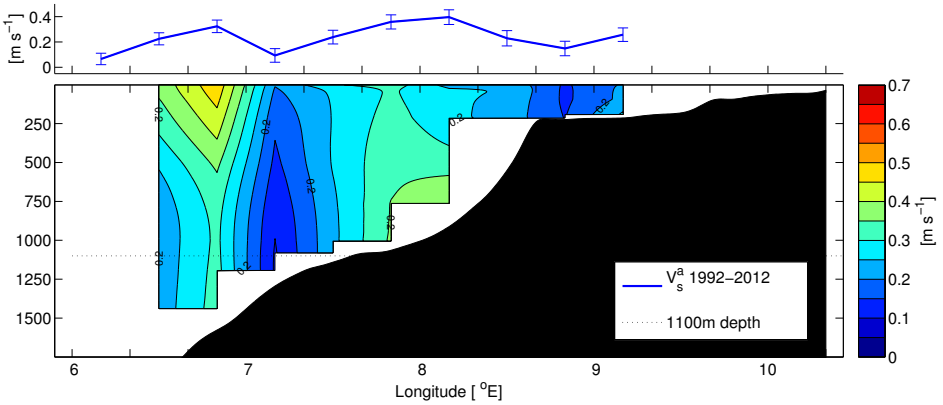

Figure 3.13: Geostrophic velocity for winter using altimetry, see caption of Figure 3.12.

Winter v_g^a is presented in Figure 3.13 where the upper panel presents v_s^a, and the lower presents the v_g^a cross section. The maximum current is 0.46 m s^{-1} close to the surface at 6.8°E, the same point where v_s^a have a local maximum. Below this v_g^a maxima decrease with depth, but still exceed 0.30 m s^{-1} at 6.8°E through the whole column. Between 7 and 7.3°E v_g^a decrease to below 0.20 m s^{-1} for most of the water column, and have a minimum of 0.10 m s^{-1} below 1000 m depth. Over the upper slope the maximum velocity is found below 700 m depth at 8°E with speeds exceeding 0.35 m s^{-1}. The rest of the area has $v_g^a \geq 0.25$ m s^{-1}. From 8°E the velocity decreases to less than 0.15 m s^{-1} towards 9°E. The vertical velocity gradients for the upper 300 m are globally small, and the strongest vertical gradient is found in the upper 400 m west of 7°E. Another notable vertical gradient is also seen form 400 m and down to the bottom at 8.1°E.

3.3 Volume transport

Volume transport for the two branches of the WSC, and total transport of AW for the whole section (As defined by Table 2.4), are estimated from the current meter data, altimetry, and hydrography (Figure 3.14). The solid lines are calculated from v_s^c, dashed lines are from v_s^a, and red and blue colors represent summer and winter respectively. The two branches are bound within the two black boxes in Figure 3.1, where the barotropic WSC branch is the eastern box, and the eastern baroclinic WSC branch (Teigen et al., 2011) is the western box. Boundaries are 6.3 to 7.5°E, and 7.5 to 9°E, and can also be seen in Figure 3.1c. All available data are used within each box when calculating the volume transport for the two branches, and the areas are fixed for all periods for consistency. When calculating total volume transport of AW the definition from Table 2.4 is used as boundary. The volume transports based on v_g^a and v_g^c data are denoted V_T^a and V_T^c respectively.

A time series of seasonal volume transport in the eastern baroclinic branch is shown in Figure 3.14a. It is seen that the volume transport for winter is higher than summer for all periods for both V_T^a and V_T^c. A steady increase in volume transport also seen in winter for the eastern baroclinic branch, while the summer shows a more steady transport with a slightly lower transport in the second period. The relative decrease

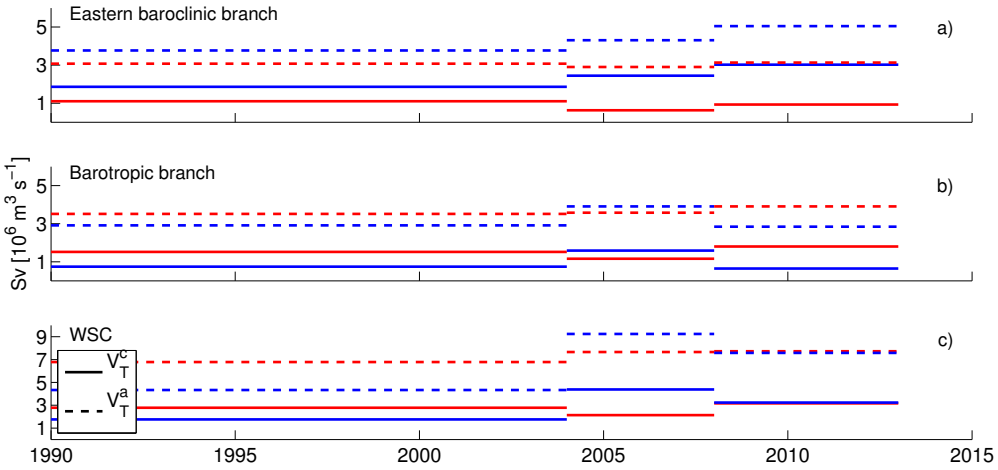

Figure 3.14: Volume transport (V_T) of the WSC for the three periods. Solid lines are calculated from v_s^c, dashed lines are from v_s^a, and red and blue colors represent summer and winter respectively. Note the difference in scale between (a-b), and (c).

in volume transport in the second period versus the average transport of the first and third period is 0.3 Sv and 0.2 Sv for V_T^c and V_T^a. Figure 3.14b presents V_T^a and V_T^c for the barotropic branch of the WSC. For V_T^a it is seen that the summer has a small but steady increase from $V_T^a = 3.51$ to 3.91 Sv. Winter V_T^a have a maximum value of 3.9 Sv in the second period, while the first and third period have a calculated $V_T^a \approx 2.9$ Sv. A similar picture is seen in V_T^c for winter with an increase of 0.7 Sv in the second period relative to the first and third period. The volume transport of AW for the three periods is presented in Figure 3.14c. A steady increase is seen in V_T^a for summer, with an increase from 6.8 to 7.7 Sv from the first to the third period. For winter the first period has a relatively low $V_T^a = 4.3$ Sv, but this increases to 9.2 Sv in the second period before it decreases to 7.6 Sv in the third period. The maximum V_T^c is found in winter during the second period, and is equal to V_T^a for the first winter period. Furthermore the lowest V_T^c of 0.6 Sv is found in winter for the first period. Summer does not show the same steady increase as the V_T^a for summer show. A small decrease in V_T^c is seen from the first to the second period before V_T^c increases again to 3.2 Sv, the same as winter.

CHAPTER 4

DISCUSSION

Here, the physical properties of the climatological CTD section are discussed, together with the three anomaly periods (1956-2003; 2004-2007; 2008-2013) and their features. Then, v_s^a and v_s^c are compared together with the calculated geostrophic velocity sections along 78.83°N. Furthermore, the temporal development in volume transport of the WSC during the different anomaly periods is discussed.

4.1 Hydrographic sections

A major part of the hydrographic profiles considered in this study are collected after 2000. The resulting climatology sections are therefore expected to be biased towards the conditions between 2000 and 2013. This is especially true for the winter season where 74 out of 82 profiles are collected after 2000 (Figure 2.4a). A bias towards this period is not necessarily a disadvantage as current meter and altimetry data is available between 1997 to 2012 and 1992 to 2012, respectively.

By comparing the total climatology (Figure 3.1) with the summer climatology (Figure 3.2) it is observed that the differences between the two sections are small. The temperature of the upper 100 m west of the shelf break of the total climatology is 0.4 °C lower relative to the summer climatology. This difference stems from adding the low surface temperature winter profiles to the warmer summer profiles. The temperature differences between the total and summer section decrease deeper down. This reflects the importance of heat exchange with the atmosphere with warming (cooling) of the WSCs surface layer during summer (winter). The total climatology carries the main features in salinity as the summer section, but features like the water with salinity higher than 35.1 psu is lost to the lower salinity in the profiles. Hence, the total climatology is dominated by the summer signal.

Summer

A comparison is possible between the summer climatology (Figure 3.2) and a climatological study by Saloranta and Haugan (2001) for the same section between 1960 and 2000. It is demonstrated in both data sets that from below the surface layer and down to between 300 and 400, and from 6 to 9.5°E, the water mass mainly consists of AW (Defined by $\theta < 2\,^{\circ}\mathrm{C}$ and $S > 34.9$ psu). The deepening of the 2 °C contour is also seen from 6°E towards the shelf break. Below a thin surface layer, AW is the dominating water mass over the shelf between 9 and 10°E(Figure 3.4(a,c and, e) and Plate 2 inSaloranta and Haugan (2001)). A less stratified part over the upper slope and a more stratified water column to the west is also seen by Cokelet et al. (2008) during a cruise in October/November 2001. Even though the section stems from the late summer period, the section also have similarities with the winter structure such as a colder surface layer and isopycnals originating from the AW core reaching the surface allows efficient cooling through isopycnal diffusion processes(Teigen et al., 2011).

The Polar Front (PF) separating the AW from the WSC and the water masses of the SPC is seen over the shelf (For instance Figure 3.1). In CTD sections presented by Saloranta and Svendsen (2001), Walczowski et al. (2005), and Walczowski (2013) the PF is seen as a distinct density front. Due to the non stationarity of the front it is smoothed out in the climatological sections presented here. The front is more visible in the three anomaly periods (For instance Figure 3.5 and Figure 3.6).

Winter

A CTD cross section from 1989 of the WSC over the shelf and slope outside the mouth of Isfjorden is presented by Boyd and D'Asaro (1994). They show a submerged AW core between 50 and 150 m depth, and the same is seen in winter in both Figure 3.3, Figure 3.4, and Figure 3.6. In Figure 3.5 the AW core is both larger and is seen higher up in the water column, all the way to the surface. The difference in temperature between Boyd and D'Asaro (1994) and the results of this work stems partly from cooling since the Boyd and D'Asaro (1994) is ≈ 100 km south of 78.83°N. Based on the estimated along shelf temperature gradients (Saloranta and Haugan, 2004) an expected along slope temperature difference for the AW layer (0 and 250 m) in the WSC is estimated to be approximately $-0.40\,^{\circ}\mathrm{C}$ (or $-0.31\,^{\circ}\mathrm{C}$ for the 0 and 500 m layer). In addition the section from Boyd and D'Asaro (1994) is collected in January-February (early winter), while the winter data in this work stems from April and May (late winter). Concurrent winter sections collected in April 2008 and 2009 is presented by Teigen (2011). They show a distinct two separated cores with temperature exceeding 3.5 °C, one in the eastern baroclinic and one in the barotropic branch.

Processes contributing to the winter time cooling of the WSC are not fully understood. Saloranta and Haugan (2004) show that the heat loss in the WSC between 100 to 500 m depth is 2.5 to 3 times larger than the heat loss in the surface, implying horizontal transport of heat both on- and off-shore is a major factor. Teigen et al. (2011) argue that isopycnal eddy diffusion from the AW core to the surface has a significant cooling impact. The climatological winter density field (Figure 3.3), and all three winter anomaly periods, have density contours favoring this mechanism as the $27.8\,\mathrm{kg\,m^{-3}}$ contour line is seen to connect with the surface west of 7°E. The

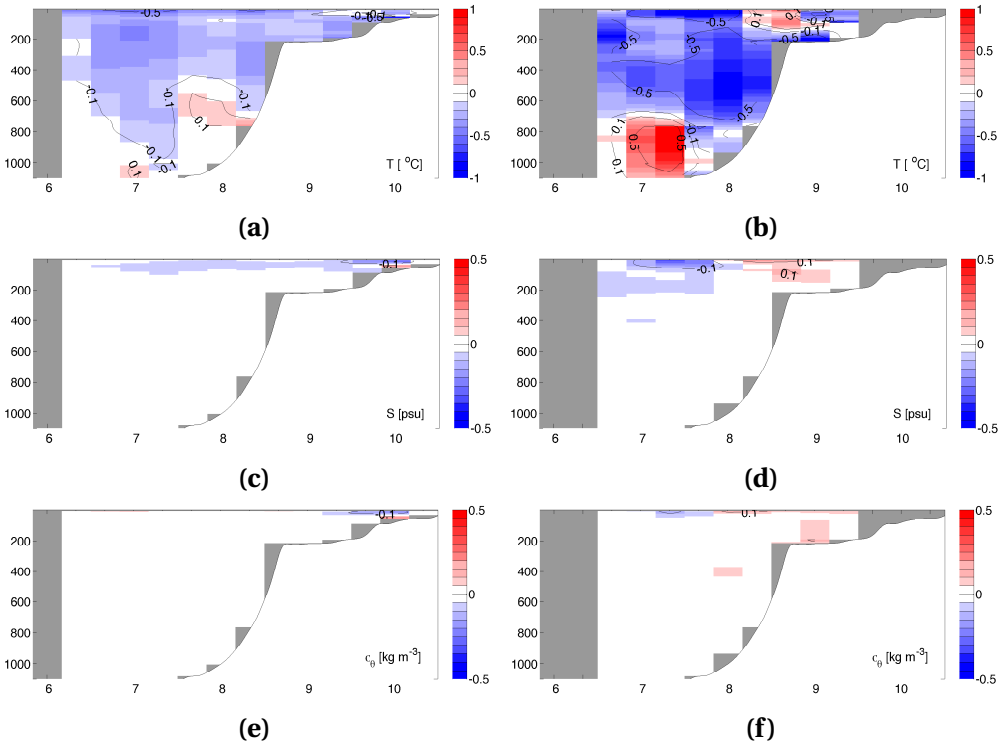

Figure 4.1: Difference between 1st period and seasonal climatologies (2008-2013 - Full seasonal dataset). Red and blue colors indicate positive and negative anomalies respectively The shaded areas represent areas without data. The bathymetry is plotted as a black line.

same density sections have weak density gradients over the shelf break 8.7°E, and this makes it possible for heat exchange across the TS front at the shelf break. This is due to vorticity waves set up by the episodic sufficient horizontal velocity shear between the barotropic core and the shelf water (Nilsen et al., 2006; Teigen et al., 2010).

Anomaly periods

On the shorter time scale the three anomaly periods are expected to show some similar features, and also reveal differences from the seasonal climatologies presented in this work. By subtracting the seasonal climatologies from each of the three shorter periods, variability in the WSC becomes clearer, This is plotted in Figures 4.1, 4.2, and 4.3.

The temperature section of the first winter period (Figure 3.4b) shows the same two-core ($T \geq 3\,°C$) structure as Teigen et al. (2011) even with the temporal difference between the data sets. The two cores ($T \geq 3\,°C$) are not seen in winter for the second and third period as the whole AW area is dominated by water warmer than 3 °C. A large core of water warmer than 3.5 °C is seen in the eastern baroclinic branch. The warm anomaly period presented in Figure 4.2 where (a) and (b) show a significant positive temperature anomaly from the surface and down to 800 m, and over the shelf. In the same period, warm water was also measured in the Isfjorden system on the west coast of Spitsbergen, indicating that the WSS was flooded with warm water (Pavlov et al., 2013). When this warm water occupies the fjords, this may stall or prevent

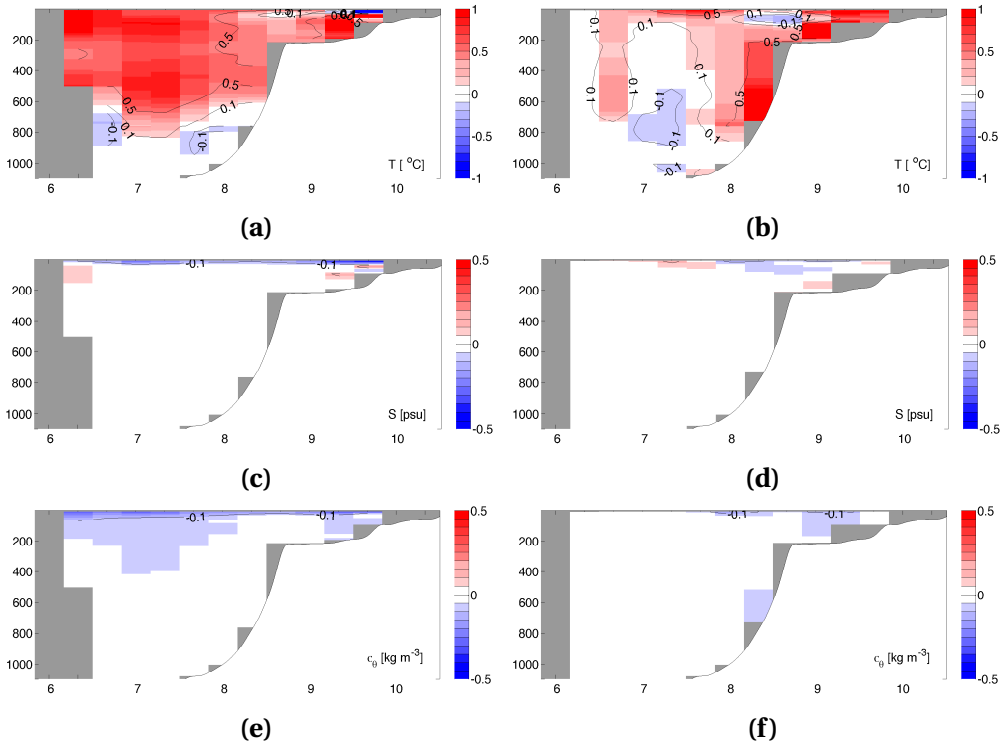

Figure 4.2: Difference between 2nd period and seasonal climatologies (2008-2013 - Full seasonal dataset). See also caption to Figure 4.1.

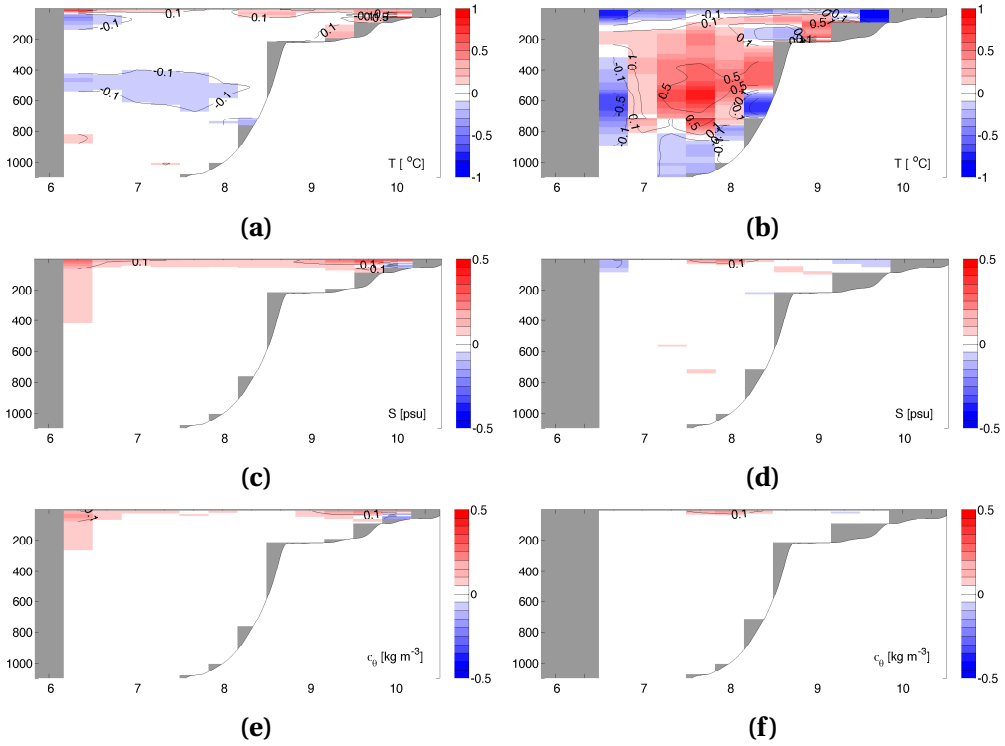

Figure 4.3: Difference between 3rd period and seasonal climatologies (2008-2013 - Full seasonal dataset). See also caption to Figure 4.1.

freezing of sea ice during winter. A possible contributor to this intrusion of warm water on the shelf is a long period of northerly winds during winter 2005/2006 causing coastal upwelling west of Spitsbergen (Cottier et al., 2007). In winter for the second period the horizontal density gradients shifts from positive to negative close to the slope (Figure 3.5f and Figure 4.2f). This difference is seen as the colder water usually seen close the slope below 600 m depth east of the AW core is replaced by AW.

A large part of the warm AW, however, will end up in the Arctic Ocean through the Yermak and Svalbard branches (Manley, 1995). Warm anomalies like the one described in the second period may have significant impact on the sea ice cover. By assuming a constant cooling of the WSC core, a significant increase in water temperature will leave more oceanic heat available for melting sea ice. Indications of this are seen in Onarheim et al. (2014) where the sea ice concentration north of Svalbard experienced a strong decrease during winter in the middle of the last decade. The loss of sea ice was consistent with a warming of AW entering the AO by $0.03\,^{\circ}\mathrm{C\,yr^{-1}}$. The same order of magnitude was found by Beszczynska-Möller et al. (2012), and corresponds with the anomaly sections calculated in this work (Figure 3.7). It is important to point out that sea ice cover time series is twice as long as the time series from the AWI array. This will bias the temperature trend from Beszczynska-Möller et al. (2012) towards the warmer 2000s. The warm water anomaly in the section studied here is not necessarily confined to melting sea ice north of Svalbard. Such anomalies can be transported over longer distances. A small WSC warm anomaly detected in the FS during winter 1999 was detected along the Laptev Sea Slope in winter 2004 showing a shoaling and deepening of the 2 °C contour (Polyakov et al., 2005). A warm anomaly in the upper 300 to 400 m is visible in the second period (Figure 4.2a), which has a significant impact on the buoyancy in this depth interval.

4.2 Geostrophic velocity and Volume transport

Current meters vs. Altimetry

Figure 3.8 compares v_s^a and v_s^c, which show that they have few similarities. In general v_s^c can be considered closer to the true v_s based on its derivation. The wave shape and strength of v_s^a are not seen in other studies of the WSC (Fahrbach et al., 2001; Walczowski et al., 2005; Beszczynska-Möller et al., 2012). Even with the wave pattern removed, v_s^a would still increase strongly towards the east. This is seen in the MDT which is plotted in Figure 4.4 together with the MDT needed to represent v_s^c, called MDT^c. The difference is clear between the too steep and irregular, slope of the MDT compared to the MDC^c. A filtering of the Geoid could be able to remove the irregular pattern, but not the too steep eastward slope. A smoothening of the geoid using a 80 km gaussian filter was done by Johannessen et al. (2014) and proved good results for the final calculation of the MDT.

Geostrophic velocity sections

The v_g^c of the barotropic branch in Figure 3.9 compares well for both speed and structure to an LADCP section collected along 78.83°N during June/July 2003 by Wal-

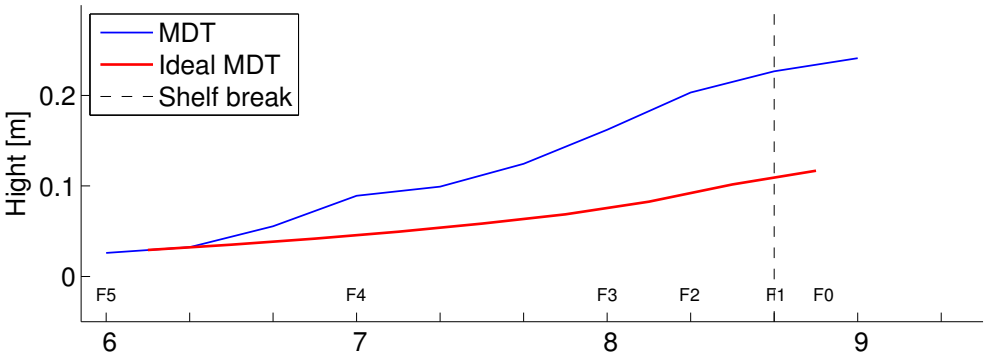

Figure 4.4: MDT and ideal MDT calculated from the first part of the RHS of (2.4). The blue line is the MDT calculated from altimetry and the red line is the ideal MDT from in-situ current meters.

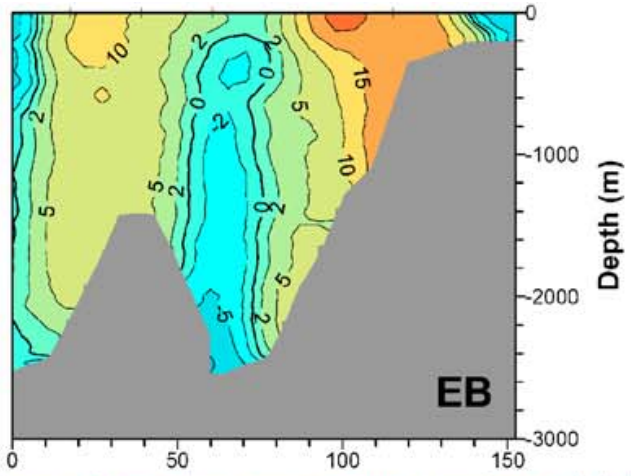

Figure 4.5: LADCP section across 78.83°N during June/July 2003, 6°E is approximately at 65 km. Velocity is given in $m\,s^{-1}$ (Adopted from Walczowski et al. (2005)).

czowski et al. (2005), and adopted in Figure 4.5.

The baroclinic current set up by the negative density gradient between 7.7°E and the shelf break explain the maximum v_s^c west of the barotropic branch (Figure 3.2c). The Yermak Branch is seen west of 6°E in the LADCP section, but not seen in Figure 3.9. No direct current measurement is found for comparison for winter. The density section (Figure 3.3c) shows a density gradient acting against the northward flowing v_s^c. This induces a negative current in the surface during winter between F2 and F3 (Figure 3.10). A similar density gradient is seen in Teigen (2011) suggesting that the result in Figure 3.10 represents a physical feature of the WSC. The total AW volume transport through the AWI array varies with several Sv, but the annual means are close to 3 Sv. This compares to the winter which varies between 1.8 and 4.4 Sv during the three anomaly periods. The lost area with an assumed transport of 0.4 Sv comes in addition. The calculation of v_g^a shown in Figure 3.12 and 3.13 are dominated by the strong v_s^a. The density field is not strong enough to adjust the mismatch between v_s^c and v_s^a.

Volume transport (V_T)

The same baroclinic hydrographic field is used to estimate both volume transport estimated from v_g^a (V_T^a) and v_g^c (V_T^c). This causes the differences between the two volume transport estimates to be a product of v_s^a and v_s^c. As seen from Figure 3.14, V_T^a is too high due to the higher v_s^a. The same v_s^a is used for all three anomaly periods and therefore the trends seen are products of hydrography.

The eastern baroclinic branch has a steady increase through all three winter periods. The first period's density section have weaker horizontal density gradients compared to the third period and the winter climatology. In addition the first winter section consists of few CTD profiles. Due to this the V_T estimate from the first winter period is expected to be the least reliable of all V_T estimates. The 2 °C contour is also seen to deepen from the first to the third periods. This allows a negative horizontal density gradient deeper down in the water column contributing to an increase in baroclinic velocity. Only small change is seen during summer, with a minimum V_T found during the second period. The high temperatures during this period appear at the same time as V_T is reduced by 0.2 Sv for both V_T^a and V_T^c. The weaker horizontal density gradients during the anomaly period cause this decrease. Small relative changes between V_T^a and V_T^c imply a stable barotropic v_s contribution to the volume transport. The calculated volume transports (Figure 3.14) are lower compared to Beszczynska-Möller et al. (2012) estimates which range between 4 and 6 Sv. The results, however, are not fully comparable as the eastern baroclinic branch is not fully resolved in the hydrographic section used here.

The barotropic branch has a less stable volume transport in the three anomaly periods, and the expected stable transport of 1.8 ± 0.1 Sv from Beszczynska-Möller et al. (2012) is not reached for V_T^c. The transport for summer and winter is within 1.2 and 1.8 Sv, and 0.6 and 1.6 Sv, respectively. This may be partly due to the lost data bound below 250 m depth and between 8.3°E and the WSS due to the chosen grid. This missing area can be approximated by a rectangle with area $250\,\mathrm{m} \times 10 \times 10^3\,\mathrm{m} = 2.5 \times 10^4\,\mathrm{m}^2$. Choosing a range for $v_g = 0.10$ to $0.15\,\mathrm{m\,s^{-1}}$ an estimate of the volume transport in this area yields between 0.3 and 0.4 Sv, closing some of the gap between literature (Beszczynska-Möller et al., 2012) and the estimates presented here.

For the winter season an increase in V_T^c of 0.8 to 1 Sv is evident during the warm anomaly. The velocity induced by the density field during this periods contributes to this increase. In this period the mean v_s^c in the barotropic branch is also at a minimum compared to the first and third period ($0.12\,\mathrm{m\,s^{-1}}$ compared to $0.15\,\mathrm{m\,s^{-1}}$ for the first, and $0.14\,\mathrm{m\,s^{-1}}$ for the third period). A distinct increase in the northward winter transport of AW during the second is caused by a change in the density field during this period. Close to the sea floor east of the AW core the upward intruding cold water (Figure 3.3 and Figure 3.5b) is replaced by AW. This alters the horizontal winter density field from arc-shaped isopycnals, seen as the lower boundary of the AW core in the total climatology. The result is a negative horizontal density gradient across the whole section in the second period inducing a northward baroclinic

contribution to the northward v_s^c. The expected V_T^c maximum during winter (Mork and Skagseth, 2010; Beszczynska-Möller et al., 2012) is not seen in Figure 3.14c. This may be because the observed winter maxima are seen early in winter (December-February), while the hydrographic data set only contain late winter profiles (April-May, see also Figure 2.4b). The increase in V_T^c and in AW mean temperature may in addition affect the Arctic sea ice cover and contribute to a change of the AO water masses. The increase in AW temperature may contribute to a shoaling of the cold halocline protecting the sea ice. Variations of both salinity and temperature are not fully correlated (Figure 3.7 and Figure 7 in Beszczynska-Möller et al. (2012)). This allow for variations in density within the Atlantic Water Layer of the AO. Karcher et al. (2011) argued using model experiments that such density anomalies may prevail within the AO and therefore decrease the Denmark Strait overflow.

4.3 Future work

An increase in the quality of the altimetry derived surface velocity would be a strong improvement. This may partly be achieved by future releases of the high quality GOCE data set to improve the Geoid. In combination with improved CryoSat-2 data for the SSH new and more reliable approximations to the surface velocity are within reach. Additional filtering or function approximation to the Geoid over shallow waters may also contribute to remove the non-realistic horizontal profiles of the surface velocity.

Increasing the hydrographic database will contribute to determine more reliable seasonal variations, especially for winter because data at this time is scarce. A redefinition of the grid used to calculate the hydrographic averages will also be helpful as the steep West Spitsbergen Slope demands a higher grid resolution than the one chosen in this work ($1/3\,^\circ$). To prevent spikes caused by low availability of data bin averaging of the hydrographic profiles may also help to remove spikes and give smoother final averages.

The effect of wind is not included in this work due to time restrictions. A comparison between the seasonal changes in v_g and the wind stress would be of value to better understand the seasonal current section. The effect of the wind stress curl is known to impact the state of the WSC and the West Spitsbergen Shelf (Cottier et al., 2007; Pavlov et al., 2013).

CHAPTER 5

CONCLUSIVE REMARKS

This work has tried to establish a climatological hydrographic status of the West Spitsbergen Current along 78.83°N using data from the period 1956 to 2013. The data has been divided into two seasons to separate the summer and winter state of the WSC. Temporal averages (1956-2003; 2004-2007; 2008-2013) have also been calculated to try to identify the hydrographic conditions during the warm anomaly of the WSC during the middle of the 2000s. Furthermore, both in-situ current meters and altimetry data have been used to determine the geostrophic current structure and speed though the section. The geostrophic current been used to estimate the volume transport through the section and the transport estimates are compared with literature.

The total and seasonal climatologies for the WSC across 78.83°N has been found to contain many of the features found in literature (Boyd and D'Asaro, 1994; Saloranta and Haugan, 2001; Saloranta and Haugan, 2004; Walczowski et al., 2005; Teigen, 2011). Both the topographically steered barotropic branch and the eastern baroclinic branch of the WSC have been identified in the hydrographic averages for both summer and winter. It must be noted that as the sections western boundary was terminated to far east, the eastern baroclinic branch is not completely resolved in the final section.

During the warm anomaly period presented by Beszczynska-Möller et al. (2012) and Polyakov et al. (2012) the Atlantic Water core was found close to the surface, and surface temperatures exceeding 3 °C were found west of the West Spitsbergen Shelf break. The temperature was high enough to increase the buoyancy of the upper 400 m of the AW. Polyakov et al. (2005) identified the signal of and earlier and smaller warm anomaly observed in the Fram Strait and later along the Laptev Sea Slope. This suggests that the warm anomaly studied here may enter and flow far into the Arctic Ocean were it will contribute to melting of an already shrinking Arctic sea ice cover. (Onarheim et al., 2014). The average temperature of the AW during the three anomaly periods was found to follow the overall warming of the WSC in the same order of magnitude as found in (Beszczynska-Möller et al., 2012).

To assess the surface velocity calculated from altimetry (v_s^a) the AWI mooring array along 78.83°N has been utilized to calculate an approximation (v_s^c) of the real surface velocity. The method for calculating the surface velocity from altimetry is adopted from Mork and Skagseth (2010). When the surface velocity calculated from altimetry and current meter data were compared, the former was found to have a high velocity and a horizontal shape not comparable to the barotropic jet found by Fahrbach et al. (2001) and Teigen et al. (2010).

Geostrophic current sections were calculated as a combination of the surface velocity and the baroclinic velocity determined from the hydrographic sections. The summer velocity section compared well to a section collected by Walczowski et al. (2005) (Adapted here as Figure 4.5) in both structure and speed. No comparable hydrographic sections were found for the late winter period, but the density field of the winter climatology share the overall features when compared to a CTD section given by Boyd and D'Asaro (1994). Due to a too high v_s^a the volume transport through the section based on altimetry was overestimated, but transport calculated using v_s^c gave reasonable values compared to Beszczynska-Möller et al. (2012). As the v_s^c was expected to be a good approximation for the true v_s, this also helped to assess the quality of the baroclinic current section calculated from the hydrographic averages. A small underestimation of the volume transport was found in the barotropic branch, but this was likely connected to the loss of a area covered due to the chosen grid. Extrapolating the lost v_g (0.10 to 0.15 m s^{-1}) for the upper 250 m down to the sea floor in this area, the volume transport estimates were nudged towards values (1.8 ± 0.1 Sv) found in Beszczynska-Möller et al. (2012).

The increase in AW volume transport during the second winter period (4.4 Sv) is caused by the increase in both v_g^c and AW area in the section. Together with the increase in AW mean temperature this may increase the heat transport into the AO and affect the hydrographic properties of the Atlantic Water inside the AO.

LIST OF FIGURES

BIBLIOGRAPHY

Aagaard, K. and Greisman, P. (1975). Toward new mass and heat budgets for the Arctic Ocean. *Journal of Geophysical Research* 80 (27), 3821–3827. ISSN: 2156-2202. DOI: 10.1029/JC080i027p03821. URL: http://dx.doi.org/10.1029/JC080i027p03821.

AVISO (2014). *AVISO Missions*. URL: http://www.aviso.oceanobs.com/en/missions.html (visited on 05/29/2014).

AVISO Products (2014). URL: http://www.aviso.oceanobs.com/en/data/products.html (visited on 05/29/2014).

Beszczynska-Möller, A., Fahrbach, E., Schauer, U., and Hansen, E. (2012). Variability in Atlantic water temperature and transport at the entrance to the Arctic Ocean, 1997–2010. *ICES Journal of Marine Science: Journal du Conseil* 69 (5), 852–863. DOI: 10.1093/icesjms/fss056. URL: http://icesjms.oxfordjournals.org/content/69/5/852.abstract.

Bourke, R. H., Weigel, A. M., and Paquette, R. G. (1988). The westward turning branch of the West Spitsbergen Current. *Journal of Geophysical Research: Oceans* 93 (C11), 14065–14077. ISSN: 2156-2202. DOI: 10.1029/JC093iC11p14065. URL: http://dx.doi.org/10.1029/JC093iC11p14065.

Boyd, T. J. and D'Asaro, E. A. (1994). Cooling of the West Spitsbergen Current: Wintertime Observations West of Svalbard. *Journal of Geophysical Research: Oceans* 99 (C11), 22597–22618. ISSN: 2156-2202. DOI: 10.1029/94JC01824. URL: http://dx.doi.org/10.1029/94JC01824.

Cokelet, E. D., Tervalon, N., and Bellingham, J. G. (2008). Hydrography of the West Spitsbergen Current, Svalbard Branch: Autumn 2001. *Journal of Geophysical Research: Oceans* 113 (C1). ISSN: 2156-2202. DOI: 10.1029/2007JC004150. URL: http://dx.doi.org/10.1029/2007JC004150.

Cottier, F. R., Nilsen, F., Inall, M. E., Gerland, S., Tverberg, V., and Svendsen, H. (2007). Wintertime warming of an Arctic shelf in response to large-scale atmospheric circulation. *Geophysical Research Letters* 34 (10). ISSN: 1944-8007. DOI: 10.1029/2007GL029948. URL: http://dx.doi.org/10.1029/2007GL029948.

ESA (2014a). *ESA European Space Agency*. URL: https://earth.esa.int/web/guest/missions/esa-operational-eo-missions (visited on 05/29/2014).

ESA (2014b). *ESA European Space Agency*. URL: http://www.esa.int/Our_Activities/Observing_the_Earth/GOCE (visited on 05/30/2014).

Fahrbach, E., Meincke, J., Østerhus, S., Rohardt, G., Schauer, U., Tverberg, V., and Verduin, J. (2001). Direct measurements of volume transports through Fram Strait. *Polar Research* 20 (2), 217–224. ISSN: 1751-8369. DOI: 10.1111/j.1751-8369.2001.tb00059.x. URL: http://dx.doi.org/10.1111/j.1751-8369.2001.tb00059.x.

Gjevik, B., Nøst, E., and Straume, T. (1994). Model simulations of the tides in the Barents Sea. *Journal of Geophysical Research: Oceans* 99 (C2), 3337–3350. ISSN: 2156-2202. DOI: 10.1029/93JC02743. URL: http://dx.doi.org/10.1029/93JC02743.

Helland-Hansen, B. and Nansen, F. (1909). *The Norwegian Sea*. 2. URL: http://web.gfi.uib.no/The%20Norwegian%20Sea/TNS.htm.

Hunegnaw, A., Siegismund, F., Hipkin, R., and Mork, K. A. (2009). Absolute flow field estimation for the Nordic seas from combined gravimetric, altimetric, and in situ data. *Journal of Geophysical Research: Oceans* 114 (C2), 1–15. ISSN: 2156-2202. DOI: 10.1029/2008JC004797. URL: http://dx.doi.org/10.1029/2008JC004797.

ILRS (2014). *ILRS International Laser Ranging Service*. URL: http://ilrs.gsfc.nasa.gov/missions/satellite_missions/current_missions/ (visited on 05/30/2014).

Ivanov, V. V., Alexeev, V. A., Repina, I., Koldunov, N. V., and Smirnov, A. (2012). Tracing Atlantic Water Signature in the Arctic Sea Ice Cover East of Svalbard. *Advances in Meteorology* 2012, 1–11. URL: http://dx.doi.org/10.1155/2012/201818.

Jakobsen, P. K., Ribergaard, M. H., Quadfasel, D., Schmith, T., and Hughes, C. W. (2003). Near-surface circulation in the northern North Atlantic as inferred from Lagrangian drifters: Variability from the mesoscale to interannual. *Journal of Geophysical Research: Oceans* 108 (C8). ISSN: 2156-2202. DOI: 10.1029/2002JC001554. URL: http://dx.doi.org/10.1029/2002JC001554.

Johannessen, J., Raj, R., Nilsen, J., Pripp, T., Knudsen, P., Counillon, F., Stammer, D., Bertino, L., Andersen, O., Serra, N., and Koldunov, N. (2014). Toward Improved Estimation of the Dynamic Topography and Ocean Circulation in the High Latitude and Arctic Ocean: The Importance of GOCE. *Surveys in Geophysics* 35 (3), 661–679. ISSN: 0169-3298. DOI: 10.1007/s10712-013-9270-y. URL: http://dx.doi.org/10.1007/s10712-013-9270-y.

Karcher, M., Beszczynska-Møller, A., Kauker, F., Gerdes, R., Heyen, S., Rudels, B., and Schauer, U. (2011). Arctic Ocean warming and its consequences for the Denmark Strait overflow. *Journal of Geophysical Research: Oceans* 116 (C2). ISSN: 2156-2202. DOI: 10.1029/2010JC006265. URL: http://dx.doi.org/10.1029/2010JC006265.

Kowalik, Z. and Proshutinsky, A. Y. (1995). Topographic enhancement of tidal motion in the western Barents Sea. *Journal of Geophysical Research: Oceans* 100 (C2), 2613–2637. ISSN: 2156-2202. DOI: 10.1029/94JC02838. URL: http://dx.doi.org/10.1029/94JC02838.

Kowalik, Z. (1994). Modeling of Topographically Amplified Diurnal Tides in the Nordic Seas. *Journal of Physical Oceanography* 24 (8), 1717–1731. DOI: 10.1175/1520-0485(1994)024<1717:MOTADT>2.0.CO;2. URL: http://dx.doi.org/10.1175/1520-0485(1994)024%3C1717:MOTADT%3E2.0.CO;2.

Lind, S. and Ingvaldsen, R. B. (2012). Variability and impacts of Atlantic Water entering the Barents Sea from the north. *Deep Sea Research Part I: Oceanographic Research Papers* 62, 70–88. ISSN: 0967-0637. DOI: http://dx.doi.org/10.1016/j.dsr.2011.12.007. URL: http://www.sciencedirect.com/science/article/pii/S0967063711002391.

Loeng, H. (1991). Features of the physical oceanographic conditions of the Barents Sea. *Polar Research* 10 (1), 5–18. ISSN: 1751-8369. DOI: 10.1111/j.1751-8369.1991.tb00630.x. URL: http://dx.doi.org/10.1111/j.1751-8369.1991.tb00630.x.

Manley, T. O. (1995). Branching of Atlantic Water within the Greenland-Spitsbergen Passage: An estimate of recirculation. *Journal of Geophysical Research: Oceans* 100 (C10), 20627–20634. ISSN: 2156-2202. DOI: 10.1029/95JC01251. URL: http://dx.doi.org/10.1029/95JC01251.

Mork, K. A. and Skagseth, Ø. (2010). A quantitative description of the Norwegian Atlantic Current by combining altimetry and hydrography. *Ocean Science* 6 (4), 901–911. DOI: 10.5194/os-6-901-2010. URL: http://www.ocean-sci.net/6/901/2010/.

Mosby, H. (1962). Water, Salt and Heat Balance of the North Polar Sea and of the Norwegian Sea. *Geofysiske Publikasjoner* (24), 289–313.

NASA (2014a). *NASA National Aeronautics and Space Administration*. URL: http://web.archive.org/web/20090730205052/http://sealevel.jpl.nasa.gov/technology/technology.html (visited on 05/29/2014).

NASA (2014b). *NASA National Aeronautics and Space Administration*. URL: http://www.nasa.gov/mission_pages/Grace/spacecraft/ (visited on 05/30/2014).

Nilsen, F., Gjevik, B., and Schauer, U. (2006). Cooling of the West Spitsbergen Current: Isopycnal diffusion by topographic vorticity waves. *Journal of Geophysical Research: Oceans* 111 (C8). ISSN: 2156-2202. DOI: 10.1029/2005JC002991. URL: http://dx.doi.org/10.1029/2005JC002991.

Onarheim, I., Smedsrud, L. H., Ingvaldsen, R., and Nilsen, F. (2014). Loss of sea ice during winter north of Svalbard. *Tellus*. In press.

Orvik, K. A. and Niiler, P. (2002). Major pathways of Atlantic water in the northern North Atlantic and Nordic Seas toward Arctic. *Geophysical Research Letters* 29 (19), 21–24. ISSN: 1944-8007. DOI: 10.1029/2002GL015002. URL: http://dx.doi.org/10.1029/2002GL015002.

Orvik, K. A. and Skagseth, Ø. (2005). Heat flux variations in the eastern Norwegian Atlantic Current toward the Arctic from moored instruments, 1995–2005. *Geophysical Research Letters* 32 (14). ISSN: 1944-8007. DOI: 10.1029/2005GL023487. URL: http://dx.doi.org/10.1029/2005GL023487.

Orvik, K. A., Skagseth, Ø., and Mork, M. (2001). Atlantic inflow to the Nordic Seas: current structure and volume fluxes from moored current meters, VM-ADCP and SeaSoar-CTD observations, 1995–1999. *Deep Sea Research Part I: Oceanographic Research Papers* 48 (4), 937–957. ISSN: 0967-0637. DOI: http://dx.doi.org/10.1016/S0967-0637(00)00038-8. URL: http://www.sciencedirect.com/science/article/pii/S0967063700000388.

Pavlov, A., Tverberg, V., Ivanov, B., Nilsen, F., Falk-Petersen, S., and Granskog, M. (2013). Warming of Atlantic Water in two west Spitsbergen fjords over the last century (1912-2009). *Polar Research* 32.

Polyakov, I. V., Beszczynska, A., Carmack, E. C., Dmitrenko, I. A., Fahrbach, E., Frolov, I. E., Gerdes, R., Hansen, E., Holfort, J., Ivanov, V. V., Johnson, M. A., Karcher, M., Kauker, F., Morison, J., Orvik, K. A., Schauer, U., Simmons, H. L., Skagseth, Ø., Sokolov, V. T., Steele, M., Timokhov, L. A., Walsh, D., and Walsh, J. E. (2005). One more step toward a warmer Arctic. *Geophysical Research Letters* 32 (17). ISSN: 1944-8007. DOI: 10.1029/2005GL023740. URL: http://dx.doi.org/10.1029/2005GL023740.

Polyakov, I. V., Pnyushkov, A. V., and Timokhov, L. A. (2012). Warming of the Intermediate Atlantic Water of the Arctic Ocean in the 2000s. *Journal of Climate* 25 (23), 8362–8370. DOI: 10.1175/JCLI-D-12-00266.1. URL: http://dx.doi.org/10.1175/JCLI-D-12-00266.1.

Quadfasel, D., Rudels, B., and Kurz, K. (1988). Outflow of dense water from a Svalbard fjord into the Fram Strait. *Deep Sea Research Part A. Oceanographic Research Papers* 35 (7), 1143–1150. ISSN: 0198-0149. DOI: http://dx.doi.org/10.1016/0198-0149(88)90006-4. URL: http://www.sciencedirect.com/science/article/pii/0198014988900064.

Rudels, B., Jones, E. P., Anderson, L. G., and Kattner, G. (1994). "On the Intermediate Depth Waters of the Arctic Ocean". *The Polar Oceans and Their Role in Shaping the Global Environment*. Ed. by O. M. Johannessen, R. D. Muench, and J. E. Overland. American Geophysical Union, 33–46. ISBN: 9781118663882. DOI: 10.1029/GM085p0033. URL: http://dx.doi.org/10.1029/GM085p0033.

Rudels, B. (1987). *On the mass balance of the Polar Ocean, with special emphasis on the Fram Strait*. Skrifter;188. Norwegian Polar Institute. ISBN: 8290307462. URL: http://brage.bibsys.no/npolar/handle/URN:NBN:no-bibsys_brage_12128.

Rudels, B., Marnela, M., and Eriksson, P. (2008). Constraints on Estimating Mass, Heat and Freshwater Transports in the Arctic Ocean: An Exercise. *Arctic–Subarctic Ocean Fluxes*. Ed. by R. R. Dickson, J. Meincke, and P. Rhines. Springer Netherlands, 315–341. ISBN: 978-1-4020-6773-0. DOI: 10.1007/978-1-4020-6774-7_14. URL: http://dx.doi.org/10.1007/978-1-4020-6774-7_14.

Saloranta, T. M. and Haugan, P. M. (2001). Interannual variability in the hydrography of Atlantic water northwest of Svalbard. *Journal of Geophysical Research: Oceans* 106 (C7), 13931–13943. ISSN: 2156-2202. DOI: 10.1029/2000JC000478. URL: http://dx.doi.org/10.1029/2000JC000478.

Saloranta, T. M. and Haugan, P. M. (2004). Northward cooling and freshening of the warm core of the West Spitsbergen Current. *Polar Research* 23 (1), 79–88. ISSN: 1751-8369. DOI: 10.1111/j.1751-8369.2004.tb00131.x. URL: http://dx.doi.org/10.1111/j.1751-8369.2004.tb00131.x.

Saloranta, T. M. and Svendsen, H. (2001). Across the Arctic front west of Spitsbergen: high-resolution CTD sections from 1998-2000. *Polar Research* 20 (2), 177–184. ISSN: 1751-8369. DOI: 10.1111/j.1751-8369.2001.tb00054.x. URL: http://dx.doi.org/10.1111/j.1751-8369.2001.tb00054.x.

Sanford, T. B., Kelly, K. A., and Farmer, D. M. (2011). Sensing the Ocean. *Physics Today* 64 (2), 24–28. DOI: 10.1063/1.3554313. URL: http://www.physicstoday.org.

Schauer, U., Beszczynska-Möller, A., Walczowski Waldemar and Fahrbach, E., Piechura, J., and Hansen, E. (2008). Variation of Measured Heat Flow Through the Fram Strait Between 1997 and 2006. *Arctic-Subarctic Ocean Fluxes*. Ed. by R. Dickson, J. Meincke, and P. Rhines. Springer Netherlands, 65–85. ISBN: 978-1-4020-6773-0. DOI: 10.1007/978-1-4020-6774-7_4. URL: http://dx.doi.org/10.1007/978-1-4020-6774-7_4.

Schauer, U., Fahrbach, E., Østerhus, S., and Rohardt, G. (2004). Arctic warming through the Fram Strait: Oceanic heat transport from 3 years of measurements. *Journal of Geophysical Research: Oceans* 109 (C6), 1–14. ISSN: 2156-2202. DOI: 10.1029/2003JC001823. URL: http://dx.doi.org/10.1029/2003JC001823.

Schlichtholz, P. and Houssais, M.-N. (1999). An inverse modeling study in Fram Strait. Part I: dynamics and circulation. *Deep Sea Research Part II: Topical Studies in Oceanography* 46 (6-7), 1083–1135. ISSN: 0967-0645. DOI: http://dx.doi.org/10.1016/S0967-0645(99)00018-1. URL: http://www.sciencedirect.com/science/article/pii/S0967064599000181.

Skagseth, Ø., Orvik, K. A., and Furevik, T. (2004). Coherent variability of the Norwegian Atlantic Slope Current derived from TOPEX/ERS altimeter data. *Geophysical Research Letters* 31 (14), 1–4. ISSN: 1944-8007. DOI: 10.1029/2004GL020057. URL: http://dx.doi.org/10.1029/2004GL020057.

Skogseth, R., Haugan, P. M., and Jakobsson, M. (2005). Watermass transformations in Storfjorden. *Continental Shelf Research* 25 (5–6), 667–695. ISSN: 0278-4343. DOI: http://dx.doi.org/10.1016/j.csr.2004.10.005. URL: http://www.sciencedirect.com/science/article/pii/S0278434304002432.

Svendsen, H., Beszczynska-Møller, A., Hagen, J., Lefauconnier, B., Tverberg, V., Gerland, S., Ørbøk, J. B., Bischof, K., Papucci, C., Zajaczkowski, M., Azzolini, R., Bruland, O., and Wiencke, C. (2002). The physical environment of Kongsfjorden–Krossfjorden, an Arctic fjord system in Svalbard. *Polar Research* 21 (1). ISSN: 1751-8369. URL: http://www.polarresearch.net/index.php/polar/article/view/6479.

Swift, J. H. and Aagaard, K. (1981). Seasonal transitions and water mass formation in the Iceland and Greenland seas. *Deep-Sea Research Part a-Oceanographic Research Papers* 28 (10), 1107–1129. DOI: 10.1016/0198-0149(81)90050-9. URL: %3CGo%20to%20ISI%3E://WOS:A1981MN97500003.

Swift, J. H. (1986). The Arctic Waters. *The Nordic Seas*. Ed. by B. G. Hurdle. Springer New York, 129–154. ISBN: 978-1-4615-8037-9. DOI: 10.1007/978-1-4615-8035-5_5. URL: http://dx.doi.org/10.1007/978-1-4615-8035-5_5.

Teigen, S. H., Nilsen, F., and Gjevik, B. (2010). Barotropic instability in the West Spitsbergen Current. *Journal of Geophysical Research: Oceans* 115 (C7), 1–18. ISSN: 2156-2202. DOI: 10.1029/2009JC005996. URL: http://dx.doi.org/10.1029/2009JC005996.

Teigen, S. H., Nilsen, F., Skogseth, R., Gjevik, B., and Beszczynska-Möller, A. (2011). Baroclinic instability in the West Spitsbergen Current. *Journal of Geophysical Research: Oceans* 116 (C7), 1–20. ISSN: 2156-2202. DOI: 10.1029/2011JC006974. URL: http://dx.doi.org/10.1029/2011JC006974.

Teigen, S. H. (2011). "Water mass exchange in the sea west of Svalbard - A process study of flow instability and vortex generated heat fluxes in the West Spitsbergen Current". PhD thesis. University of Bergen and University Center of Svalbard.

Walczowski, W. (2013). Frontal structures in the West Spitsbergen Current margins. *Ocean Science* 9 (6), 957–975. DOI: 10.5194/os-9-957-2013. URL: http://www.ocean-sci.net/9/957/2013/.

Walczowski, W. and Piechura, J. (2007). Pathways of the Greenland Sea warming. *Geophysical Research Letters* 34 (10), 1–5. ISSN: 1944-8007. DOI: 10.1029/2007GL029974. URL: http://dx.doi.org/10.1029/2007GL029974.

Walczowski, W., Piechura, J., Osinski, R., and Wieczorek, P. (2005). The West Spitsbergen Current volume and heat transport from synoptic observations in summer. *Deep Sea Research Part I: Oceanographic Research Papers* 52 (8), 1374–1391. ISSN: 0967-0637. DOI: http://dx.doi.org/10.1016/j.dsr.2005.03.009. URL: http://www.sciencedirect.com/science/article/pii/S0967063705000889.